Draft

Lecture Notes in:

FRACTURE MECHANICS

Victor E. Saouma

Dept. of Civil Environmental and Architectural Engineering

University of Colorado, Boulder, CO 80309-0428

Draft

Contents

List of Figures

List of Tables

Chapter 1

INTRODUCTION

In this introductory chapter, we shall start by reviewing the various modes of structural failure and highlight the importance of fracture induced failure and contrast it with the limited coverage given to fracture mechanics in Engineering Education. In the next section we will discuss some examples of well known failures/accidents attributed to cracking. Then, using a simple example we shall compare the failure load predicted from linear elastic fracture mechanics with the one predicted by "classical" strength of materials. The next section will provide a brief panoramic overview of the major developments in fracture mechanics. Finally, the chapter will conclude with an outline of the lecture notes.

1.1 Modes of Failures

The fundamental requirement of any structure is that it should be designed to resist mechanical failure through any (or a combination of) the following modes:

1. Elastic instability (buckling)
2. Large elastic deformation (jamming)
3. Gross plastic deformation (yielding)
4. Tensile instability (necking)
5. Fracture

Most of these failure modes are relatively well understood, and proper design procedures have been developed to resist them. However, fractures occurring after earthquakes constitute the major source of structural damage (Duga, Fisher, Buxbam, Rosenfield, Buhr, Honton and McMillan 1983), and are the least well understood.

In fact, fracture often has been overlooked as a potential mode of failure at the expense of an overemphasis on strength. Such a simplification is not new, and finds a very similar analogy in the critical load of a column. If column strength is based entirely on a strength criterion, an unsafe design may result as instability (or buckling) is overlooked for slender members. Thus failure curves for columns show a smooth transition in the failure mode from columns based on gross section yielding to columns based on instability.

By analogy, a cracked structure can be designed on the sole basis of strength as long as the crack size does not exceed a critical value. Should the crack size exceed this critical value, then

Chapter 2

PRELIMINARY CONSIDERATIONS

`Needs some minor editing!`

1 Whereas, ideally, an introductory course in *Continuum Mechanics* should be taken prior to a fracture mechanics, this is seldom the case. Most often, students have had a graduate course in *Advanced Strength of Materials*, which can only provide limited background to a solid fracture mechanics course.

2 Accordingly, this preliminary chapter (mostly extracted from the author's lecture notes in Continuum Mechanics) will partially remedy for occasional deficiencies and will be often referenced.

3 It should be noted that most, but not all, of the material in this chapter will be subsequently referenced.

2.1 Tensors

4 We now seek to generalize the concept of a vector by introducing the **tensor** (**T**), which essentially *exists to operate on vectors* **v** *to produce other vectors* (or on tensors to produce other tensors!). We designate this operation by **T**·**v** or simply **Tv**.

5 We hereby adopt the **dyadic** notation for tensors as **linear vector operators**

$$\mathbf{u} = \mathbf{T}\cdot\mathbf{v} \quad \text{or} \quad u_i = T_{ij}v_j \tag{2.1-a}$$

$$\mathbf{u} = \mathbf{v}\cdot\mathbf{S} \quad \text{where} \quad \mathbf{S} = \mathbf{T}^T \tag{2.1-b}$$

6 Whereas a tensor is essentially an operator on vectors (or other tensors), it is also a physical quantity, independent of any particular coordinate system yet specified most conveniently by referring to an appropriate system of coordinates.

7 Tensors frequently arise as physical entities whose components are the coefficients of a linear relationship between vectors.

- A fourth order tensor (such as Elastic constants) will have four free indices.

4. Derivatives of tensor with respect to x_i is written as $,i$. For example:

$$\frac{\partial \Phi}{\partial x_i} = \Phi_{,i} \quad \frac{\partial v_i}{\partial x_i} = v_{i,i} \quad \frac{\partial v_i}{\partial x_j} = v_{i,j} \quad \frac{\partial T_{i,j}}{\partial x_k} = T_{i,j,k} \tag{2.6}$$

14 Usefulness of the indicial notation is in presenting systems of equations in compact form. For instance:

$$x_i = c_{ij} z_j \tag{2.7}$$

this simple compacted equation, when expanded would yield:

$$\begin{aligned} x_1 &= c_{11}z_1 + c_{12}z_2 + c_{13}z_3 \\ x_2 &= c_{21}z_1 + c_{22}z_2 + c_{23}z_3 \\ x_3 &= c_{31}z_1 + c_{32}z_2 + c_{33}z_3 \end{aligned} \tag{2.8-a}$$

Similarly:

$$A_{ij} = B_{ip} C_{jq} D_{pq} \tag{2.9}$$

$$\begin{aligned} A_{11} &= B_{11}C_{11}D_{11} + B_{11}C_{12}D_{12} + B_{12}C_{11}D_{21} + B_{12}C_{12}D_{22} \\ A_{12} &= B_{11}C_{11}D_{11} + B_{11}C_{12}D_{12} + B_{12}C_{11}D_{21} + B_{12}C_{12}D_{22} \\ A_{21} &= B_{21}C_{11}D_{11} + B_{21}C_{12}D_{12} + B_{22}C_{11}D_{21} + B_{22}C_{12}D_{22} \\ A_{22} &= B_{21}C_{21}D_{11} + B_{21}C_{22}D_{12} + B_{22}C_{21}D_{21} + B_{22}C_{22}D_{22} \end{aligned} \tag{2.10-a}$$

15 Using indicial notation, we may rewrite the definition of the dot product

$$\boxed{\mathbf{a}\cdot\mathbf{b} = a_i b_i} \tag{2.11}$$

and of the cross product

$$\boxed{\mathbf{a}\times\mathbf{b} = \varepsilon_{pqr} a_q b_r \mathbf{e}_p} \tag{2.12}$$

we note that in the second equation, there is one free index p thus there are three equations, there are two repeated (dummy) indices q and r, thus each equation has nine terms.

2.1.2 Tensor Operations

16 The sum of two (second order) tensors is simply defined as:

$$\boxed{\mathbf{S}_{ij} = \mathbf{T}_{ij} + \mathbf{U}_{ij}} \tag{2.13}$$

2.1.3 Rotation of Axes

23 The rule for changing second order tensor components under rotation of axes goes as follow:

$$\begin{aligned} \overline{u}_i &= a_i^j u_j && \text{From Eq. ??} \\ &= a_i^j T_{jq} v_q && \text{From Eq. 2.1-a} \\ &= a_i^j T_{jq} a_p^q \overline{v}_p && \text{From Eq. ??} \end{aligned} \tag{2.20}$$

But we also have $\overline{u}_i = \overline{T}_{ip}\overline{v}_p$ (again from Eq. 2.1-a) in the barred system, equating these two expressions we obtain

$$\overline{T}_{ip} - (a_i^j a_p^q T_{jq})\overline{v}_p = 0 \tag{2.21}$$

hence

$$\boxed{\begin{array}{lcll} \overline{T}_{ip} &=& a_i^j a_p^q T_{jq} & \text{in Matrix Form} \quad [\overline{T}] = [A]^T[T][A] \\ T_{jq} &=& a_i^j a_p^q \overline{T}_{ip} & \text{in Matrix Form} \quad [T] = [A][\overline{T}][A]^T \end{array}} \tag{2.22}$$

By extension, higher order tensors can be similarly transformed from one coordinate system to another.

24 If we consider the 2D case, From Eq. **??**

$$A = \begin{bmatrix} \cos\alpha & \sin\alpha & 0 \\ -\sin\alpha & \cos\alpha & 0 \\ 0 & 0 & 1 \end{bmatrix} \tag{2.23-a}$$

$$T = \begin{bmatrix} T_{xx} & T_{xy} & 0 \\ T_{xy} & T_{yy} & 0 \\ 0 & 0 & 0 \end{bmatrix} \tag{2.23-b}$$

$$\overline{T} = A^T T A = \begin{bmatrix} \overline{T}_{xx} & \overline{T}_{xy} & 0 \\ \overline{T}_{xy} & \overline{T}_{yy} & 0 \\ 0 & 0 & 0 \end{bmatrix} \tag{2.23-c}$$

$$= \begin{bmatrix} \cos^2\alpha T_{xx} + \sin^2\alpha T_{yy} + \sin 2\alpha T_{xy} & \frac{1}{2}(-\sin 2\alpha T_{xx} + \sin 2\alpha T_{yy} + 2\cos 2\alpha T_{xy} & 0 \\ \frac{1}{2}(-\sin 2\alpha T_{xx} + \sin 2\alpha T_{yy} + 2\cos 2\alpha T_{xy} & \sin^2\alpha T_{xx} + \cos\alpha(\cos\alpha T_{yy} - 2\sin\alpha T_{xy} & 0 \\ 0 & 0 & 0 \end{bmatrix} \tag{2.23-d}$$

alternatively, using $\sin 2\alpha = 2\sin\alpha\cos\alpha$ and $\cos 2\alpha = \cos^2\alpha - \sin^2\alpha$, this last equation can be rewritten as

$$\boxed{\begin{Bmatrix} \overline{T}_{xx} \\ \overline{T}_{yy} \\ \overline{T}_{xy} \end{Bmatrix} = \begin{bmatrix} \cos^2\theta & \sin^2\theta & 2\sin\theta\cos\theta \\ \sin^2\theta & \cos^2\theta & -2\sin\theta\cos\theta \\ -\sin\theta\cos\theta & \cos\theta\sin\theta & \cos^2\theta - \sin^2\theta \end{bmatrix} \begin{Bmatrix} T_{xx} \\ T_{yy} \\ T_{xy} \end{Bmatrix}} \tag{2.24}$$

2.1.4 Trace

25 The **trace** of a second-order tensor, denoted tr $\mathbf{T}$ is a scalar invariant function of the tensor and is defined as

$$\boxed{\text{tr } \mathbf{T} \equiv T_{ii}} \tag{2.25}$$

Thus it is equal to the sum of the diagonal elements in a matrix.

2.2 Kinetics

2.2.1 Force, Traction and Stress Vectors

32 There are two kinds of **forces** in continuum mechanics

body forces: act on the elements of volume or mass inside the body, e.g. gravity, electromagnetic fields. $d\mathbf{F} = \rho \mathbf{b} \mathrm{d}Vol$.

surface forces: are contact forces acting on the free body at its bounding surface. Those will be defined in terms of **force per unit area.**

33 The surface force per unit area acting on an element dS is called **traction** or more accurately **stress vector**.

$$\int_S \mathbf{t} \mathrm{d}S = \mathbf{i} \int_S t_x \mathrm{d}S + \mathbf{j} \int_S t_y \mathrm{d}S + \mathbf{k} \int_S t_z \mathrm{d}S \tag{2.34}$$

Most authors limit the term traction to an actual bounding surface of a body, and use the term **stress vector** for an imaginary interior surface (even though the state of stress is a tensor and not a vector).

34 The traction vectors on planes perpendicular to the coordinate axes are particularly useful. When the vectors acting at a point on three such mutually perpendicular planes is given, the **stress vector** at that point on any other arbitrarily inclined plane can be expressed in terms of the first set of tractions.

35 A **stress**, Fig 2.1 is a second order cartesian tensor, σ_{ij} where the 1st subscript (i) refers to

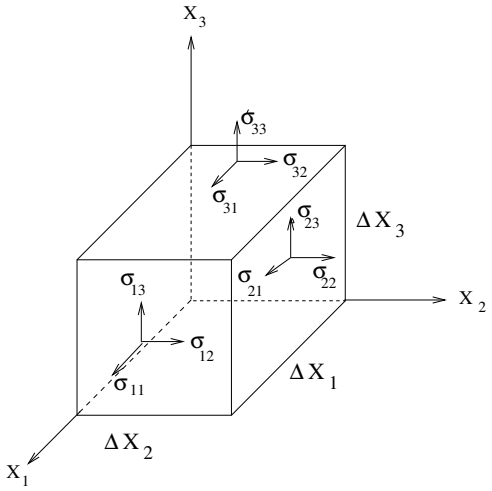

Figure 2.1: Stress Components on an Infinitesimal Element

the direction of outward facing normal, and the second one (j) to the direction of component force.

$$\boldsymbol{\sigma} = \sigma_{ij} = \begin{bmatrix} \sigma_{11} & \sigma_{12} & \sigma_{13} \\ \sigma_{21} & \sigma_{22} & \sigma_{23} \\ \sigma_{31} & \sigma_{32} & \sigma_{33} \end{bmatrix} = \begin{Bmatrix} \mathbf{t}_1 \\ \mathbf{t}_2 \\ \mathbf{t}_3 \end{Bmatrix} \tag{2.35}$$

Chapter 3

ELASTICITY BASED SOLUTIONS FOR CRACK PROBLEMS

3.1 Introduction

1 This chapter will present mathematically rigorous derivations of some simple elasticity problems. All the theoretical basis required to follow those derivations have been covered in the previous chapter. A summary of problems to be investigated is shown in Table 3.1.

3.2 Circular Hole, (Kirsch, 1898)

2 Analysing the infinite plate under uniform tension with a circular hole of diameter a, and subjected to a uniform stress σ_0, Fig. 3.1.

3 The peculiarity of this problem is that the far-field boundary conditions are better expressed in cartesian coordinates, whereas the ones around the hole should be written in polar coordinate system.

4 We will solve this problem by replacing the plate with a thick tube subjected to two different set of loads. The first one is a thick cylinder subjected to uniform radial pressure (solution of which is well known from *Strength of Materials*), the second one is a thick cylinder subjected to both radial and shear stresses which must be compatible with the traction applied on the rectangular plate.

Problem	Coordinate System	Real/Complex	Solution	Date
Circular Hole	Polar	Real	Kirsh	1898
Elliptical Hole	Curvilinear	Complex	Inglis	1913
Crack	Cartesian	Complex	Westergaard	1939
V Notch	Polar	Complex	Willimas	1952
Dissimilar Materials	Polar	Complex	Williams	1959
Anisotropic Materials	Cartesian	Complex	Sih	1965

Table 3.1: Summary of Elasticity Based Problems Analysed

1. Outer boundaries: around an infinitely large circle of radius b inside a plate subjected to uniform stress σ_0, the stresses in polar coordinates are obtained from *Strength of Materials*

$$\begin{bmatrix} \sigma_{rr} & \sigma_{r\theta} \\ \sigma_{r\theta} & \sigma_{\theta\theta} \end{bmatrix} = \begin{bmatrix} \cos\theta & -\sin\theta \\ \sin\theta & \cos\theta \end{bmatrix} \begin{bmatrix} \sigma_0 & 0 \\ 0 & 0 \end{bmatrix} \begin{bmatrix} \cos\theta & -\sin\theta \\ \sin\theta & \cos\theta \end{bmatrix}^T \tag{3.7}$$

yielding (recalling that $\sin^2\theta = 1/2\sin 2\theta$, and $\cos^2\theta = 1/2(1+\cos 2\theta)$).

$$(\sigma_{rr})_{r=b} = \sigma_0\cos^2\theta = \frac{1}{2}\sigma_0(1+\cos 2\theta) \tag{3.8-a}$$

$$(\sigma_{r\theta})_{r=b} = \frac{1}{2}\sigma_0\sin 2\theta \tag{3.8-b}$$

$$(\sigma_{\theta\theta})_{r=b} = \frac{\sigma_0}{2}(1-\cos 2\theta) \tag{3.8-c}$$

For reasons which will become apparent later, it is more convenient to decompose the state of stress given by Eq. 3.8-a and 3.8-b, into state I and II:

$$(\sigma_{rr})^I_{r=b} = \frac{1}{2}\sigma_0 \tag{3.9-a}$$

$$(\sigma_{r\theta})^I_{r=b} = 0 \tag{3.9-b}$$

$$(\sigma_{rr})^{II}_{r=b} = \frac{1}{2}\sigma_0\cos 2\theta \leftarrow \tag{3.9-c}$$

$$(\sigma_{r\theta})^{II}_{r=b} = \frac{1}{2}\sigma_0\sin 2\theta \leftarrow \tag{3.9-d}$$

Where state I corresponds to a thick cylinder with external pressure applied on $r = b$ and of magnitude $\sigma_0/2$. Hence, only the last two equations will provide us with boundary conditions.

2. Around the hole: the stresses should be equal to zero:

$$(\sigma_{rr})_{r=a} = 0 \leftarrow \tag{3.10-a}$$

$$(\sigma_{r\theta})_{r=a} = 0 \leftarrow \tag{3.10-b}$$

12 Upon substitution in Eq. 3.6 the four boundary conditions (Eq. 3.9-c, 3.9-d, 3.10-a, and 3.10-b) become

$$-\left(2A + \frac{6C}{b^4} + \frac{4D}{b^2}\right) = \frac{1}{2}\sigma_0 \tag{3.11-a}$$

$$\left(2A + 6Bb^2 - \frac{6C}{b^4} - \frac{2D}{b^2}\right) = \frac{1}{2}\sigma_0 \tag{3.11-b}$$

$$-\left(2A + \frac{6C}{a^4} + \frac{4D}{a^2}\right) = 0 \tag{3.11-c}$$

$$\left(2A + 6Ba^2 - \frac{6C}{a^4} - \frac{2D}{a^2}\right) = 0 \tag{3.11-d}$$

66 Thus we can define

$$a_n = \frac{A_n}{B_n} = -\frac{\cos(\lambda_n - 1)\alpha}{\cos(\lambda_n + 1)\alpha} = -\frac{\omega \sin(\lambda_n - 1)\alpha}{\sin(\lambda_n + 1)\alpha} \tag{3.77-a}$$

$$b_n = \frac{C_n}{D_n} = -\frac{\sin(\lambda_n - 1)\alpha}{\sin(\lambda_n + 1)\alpha} = -\frac{\omega \cos(\lambda_n - 1)\alpha}{\cos(\lambda_n + 1)\alpha} \tag{3.77-b}$$

these ratios are equal to $1/3$ and -1 respectively for $\alpha = \pi$ and $\lambda = 1/2$. and

$$F(\theta) = \sum \left[a_n \left(\sin \frac{3}{2}\theta + \sin \frac{1}{2}\theta \right) + b_n \left(\frac{1}{3} \cos \frac{3}{2}\theta + \cos \frac{1}{2}\theta \right) \right] \tag{3.78}$$

67 The stresses are obtained by substituting

$$\sigma_{rr} = \sum \left[\frac{b_n}{\sqrt{r}} \left(\frac{5}{4} \cos \frac{\theta}{2} - \frac{1}{4} \cos \frac{3\theta}{2} \right) + \frac{a_n}{\sqrt{r}} \left(-\frac{5}{4} \sin \frac{\theta}{2} + \frac{3}{4} \sin \frac{3\theta}{2} \right) \right] \tag{3.79-a}$$

$$\sigma_{\theta\theta} = \sum \left[\frac{b_n}{\sqrt{r}} \left(\frac{3}{4} \cos \frac{\theta}{2} + \frac{1}{4} \cos \frac{3\theta}{2} \right) + \frac{a_n}{\sqrt{r}} \left(-\frac{3}{4} \sin \frac{\theta}{2} - \frac{3}{4} \sin \frac{3\theta}{2} \right) \right] \tag{3.79-b}$$

$$\sigma_{r\theta} = \sum \left[\frac{b_n}{\sqrt{r}} \left(\frac{1}{4} \sin \frac{\theta}{2} + \frac{1}{4} \sin \frac{3\theta}{2} \right) + \frac{a_n}{\sqrt{r}} \left(\frac{1}{4} \cos \frac{\theta}{2} + \frac{3}{4} \cos \frac{3\theta}{2} \right) \right] \tag{3.79-c}$$

68 These equations can be further simplified into

$$\sigma_{rr} = \sum \left[\frac{b_n}{\sqrt{r}} \cos \frac{\theta}{2} \left(1 + \sin^2 \frac{\theta}{2} \right) + \frac{a_n}{\sqrt{r}} \left(-\frac{5}{4} \sin \frac{\theta}{2} + \frac{3}{4} \sin \frac{3\theta}{2} \right) \right] \tag{3.80-a}$$

$$\sigma_{\theta\theta} = \sum \left[\frac{b_n}{\sqrt{r}} \cos \frac{\theta}{2} \left(1 - \sin^2 \frac{\theta}{2} \right) + \frac{a_n}{\sqrt{r}} \left(-\frac{3}{4} \sin \frac{\theta}{2} - \frac{3}{4} \sin \frac{3\theta}{2} \right) \right] \tag{3.80-b}$$

$$\sigma_{r\theta} = \sum \left[\frac{b_n}{\sqrt{r}} \sin \frac{\theta}{2} \cos^2 \frac{\theta}{2} + \frac{a_n}{\sqrt{r}} \left(\frac{1}{4} \cos \frac{\theta}{2} + \frac{3}{4} \cos \frac{3\theta}{2} \right) \right] \tag{3.80-c}$$

69 Finally, it can be shown that the displacements will be given by

$$\begin{aligned} u = \frac{1}{2\mu} \sum Re \Big\{ & a_n r^{\lambda_n} \left[(\kappa + \lambda_n \cos 2\alpha + \cos 2\lambda_n \alpha) \cos \lambda_n \theta - \lambda_n \cos(\lambda_n - 2)\theta \right] \\ & - b_n r^{\xi_n} \left[(\kappa + \xi_n \cos 2\alpha - \cos 2\xi_n \alpha) \sin \xi_n \theta - \xi_n \sin(\xi_n - 2)\theta \right] \Big\} \end{aligned} \tag{3.81-a}$$

$$\begin{aligned} v = \frac{1}{2\mu} \sum Re \Big\{ & a_n r^{\lambda_n} \left[(\kappa - \lambda_n \cos 2\alpha - \cos 2\lambda_n \alpha) \sin \lambda_n \theta + \lambda_n \sin(\lambda_n - 2)\theta \right] \\ & + b_n r^{\xi_n} \left[(\kappa - \xi_n \cos 2\alpha + \cos 2\xi_n \alpha) \cos \xi_n \theta + \xi_n \cos(\xi_n - 2)\theta \right] \Big\} \end{aligned} \tag{3.81-b}$$

70 This solution can be compared with Westergaard's solution by comparing Equations 3.55-a and 3.56-a with Eq. 3.80-a; Eq. 3.55-b and 3.56-b with Eq. 3.80-b; and Eq. 3.55-c and 3.56-c with Eq. 3.80-c for $n = 1$. From this we observe that

$$\boxed{\begin{aligned} b_1 &= \frac{K_I}{\sqrt{2\pi}} \\ a_1 &= \frac{K_{II}}{\sqrt{2\pi}} \end{aligned}} \tag{3.82}$$

or $F_1'(\pi) = F_2'(-\pi) = 0$

- Continuity of $\sigma_{\theta\theta}$ at the interface, $\theta = 0$

$$A_1 + B_1 = A_2 + B_2 \tag{3.87}$$

- Continuity of $\sigma_{r\theta}$ at $\theta = 0$ along the interface

$$(\lambda-1)C_1 + (\lambda+1)D_1 = -(\lambda-1)C_2 - (\lambda+1)D_2 \tag{3.88}$$

- Continuity of displacements (u_r, u_θ) at the interface. Using the polar expression of the displacements

$$u_r^i = \frac{1}{2\mu_i} r^\lambda \{-(\lambda+1)F_i(\theta) + 4(1-\alpha_i)[C_i \sin(\lambda-1)\theta + A_i \cos(\lambda-1)\theta]\} \tag{3.89-a}$$

$$u_\theta^i = \frac{1}{2\mu_i} r^\lambda \{-F_i'(\theta) - 4(1-\alpha_i)[C_i \cos(\lambda-1)\theta - A_i \sin(\lambda-1)\theta]\} \tag{3.89-b}$$

where μ is the shear modulus, and $\alpha_i \equiv \frac{\nu_i}{1+\nu_i}$
we obtain

$$\frac{1}{2\mu_1}\left[-(\lambda+1)F_1(0) + 4A_1(1-\alpha_1)\right] = \frac{1}{2\mu_2}\left[-(\lambda+1)F_2(0) + 4A_2(1-\alpha_2)\right] \tag{3.90-a}$$

$$\frac{1}{2\mu_1}\left[-F_1'(0) - 4C_1(1-\alpha_1)\right] = \frac{1}{2\mu_2}\left[-F_2'(0) - 4C_2(1-\alpha_2)\right] \tag{3.90-b}$$

3.6.3 Homogeneous Equations

74 Applying those boundary conditions, will lead to 8 homogeneous linear equations (Eq. 3.85-a, 3.85-b, 3.86-b, 3.86-c, 3.87, 3.88, 3.90-a, 3.90-b) in terms of the 8 unknowns $A_1, B_1, C_1, D_1, A_2, B_2, C_2$ and D_2.

75 A nontrivial solution exists if the determinant of the 8 equations is equal to zero. This determinant[5] is equal to

$$\cot^2 \lambda\pi + \left[\frac{2k(1-\alpha_2) - 2(1-\alpha_1) - (k-1)}{2k(1-\alpha_2) + 2(1-\alpha_1)}\right]^2 = 0 \tag{3.91}$$

where $k = \frac{\mu_1}{\mu_2}$.

76 For the homogeneous case $\alpha_1 = \alpha_2$ and $k = 1$, the previous equation reduces to $\cot^2 \lambda\pi = 0$ or $\sin^2 \lambda\pi = 0$ thus we recover the same solution as the one of Eq. 3.73-b for a crack in one material:

$$\lambda = \frac{n}{2} \qquad n = 1, 2, 3, ... \tag{3.92}$$

Note that we exclude negative values of n to ensure finite displacements as the origin is approached, and the lowest eigenvalue controls.

[5] The original paper states: ... *After some algebraic simplification...*

80 Thus, Eq. 3.91 finally leads to

$$\text{Re}(\cot \lambda\pi) = 0 \tag{3.100-a}$$
$$\text{Im}(\cot \lambda\pi) = \pm\beta \tag{3.100-b}$$

we thus have two equations with two unknowns.

3.6.4 Solve for λ

81 Let us solve those two equations. Two sets of solutions are possible:

1. If from 3.99-b $\tan \lambda_r\pi = 0$ then

$$\lambda_r = n = 0, 1, 2, 3, ... \tag{3.101}$$

and accordingly from Eq. 3.100-b

$$\lambda_j = \pm\frac{1}{\pi}\coth^{-1}\beta \tag{3.102}$$

2. Alternatively, from Eq. 3.100-a $\cot \lambda_r\pi = 0 \Rightarrow \tan \lambda_r\pi = \infty$ and[6]:

$$\lambda_r = \frac{2n+1}{2} \qquad n = 0, 1, 2, 3, ... \tag{3.103-a}$$
$$\lambda_j = \pm\frac{1}{\pi}\tanh^{-1}\beta \tag{3.103-b}$$
$$= \frac{1}{2\pi}\log\left[\frac{\beta+1}{\beta-1}\right] \tag{3.103-c}$$

We note that for this case, $\lambda_j \to 0$ as $\alpha_1 \to \alpha_2$ and $k \to 1$ in β.

3.6.5 Near Crack Tip Stresses

82 Now that we have solved for λ, we need to derive expressions for the near crack tip stress field. We rewrite Eq. 3.83 as

$$\Phi(r) = \underbrace{r^{\lambda+1}}_{G(r)} F(\theta, \lambda) \tag{3.104}$$

we note that we no longer have two sets of functions, as the effect of dissimilar materials has been accounted for and is embedded in λ.

83 The stresses will be given by Eq. **??**

$$\sigma_{rr} = \frac{1}{r^2}\frac{\partial^2\Phi}{\partial\theta^2} + \frac{1}{r}\frac{\partial\Phi}{\partial r} = r^{-2}G(r)F''(\theta) + r^{-1}G'(r)F(\theta) \tag{3.105-a}$$
$$\sigma_{\theta\theta} = \frac{\partial^2\Phi}{\partial r^2} = G''(r)F(\theta) \tag{3.105-b}$$
$$\sigma_{r\theta} = \frac{1}{r^2}\frac{\partial\Phi}{\partial\theta} - \frac{1}{r}\frac{\partial^2\Phi}{\partial r\partial\theta} = r^{-2}G(r)F'(\theta) - r^{-1}G'(r)F'(\theta) \tag{3.105-c}$$

[6] Recall that $\tanh^{-1} x = \frac{1}{2}\log\frac{1+x}{1-x}$

thus,

$$\begin{aligned}\mathrm{Re}\left\{\sin\left[(\lambda_r \pm 1) + i\lambda_j\right]\theta\right\} &= \sin(\lambda_r \pm 1)\cos(\theta)\cosh\lambda_j\theta && \text{(3.114-a)}\\ \mathrm{Re}\left\{\cos\left[(\lambda_r \pm 1) + i\lambda_j\right]\theta\right\} &= \cos(\lambda_r \pm 1)\cos(\theta)\cosh\lambda_j\theta && \text{(3.114-b)}\end{aligned}$$

87 Substituting those relations in Eq. 3.112

$$\begin{aligned}\mathrm{Re}\left[F(\theta)\right] &= \underbrace{\cosh\lambda_j\theta}_{f(\theta)} && \text{(3.115-a)}\\ &\quad \underbrace{\left[A\cos(\lambda_r-1)\theta + B\cos(\lambda_r+1)\theta + C\sin(\lambda_r-1)\theta + D\sin(\lambda_r+1)\theta\right]}_{g(\theta)} && \text{(3.115-b)}\\ \mathrm{Re}\left[\Phi(r,\theta)\right] &= r^{\lambda_r+1}\cos(\lambda_j\log(r))\cosh\lambda_j\theta\\ &\quad \left[A\cos(\lambda_r-1)\theta + B\cos(\lambda_r+1)\theta\right.\\ &\quad \left.+C\sin(\lambda_r-1)\theta + D\sin(\lambda_r+1)\theta\right] && \text{(3.115-c)}\end{aligned}$$

88 For $\lambda_r = \frac{1}{2}$

$$g(\theta) = A\cos\frac{\theta}{2} + B\cos\frac{3\theta}{2} - C\sin\frac{\theta}{2} + D\sin\frac{3\theta}{2} \tag{3.116}$$

89 Applying the boundary conditions at $\theta = \pm\pi$, $\sigma_{\theta\theta} = 0$, Eq. 3.105-b $F(\theta) = 0$, that is $g_1(-\pi) = g_2(\pi)$ or

$$C = -D = -a \tag{3.117}$$

90 Similarly at $\theta = \pm\pi$, $\sigma_{r\theta} = 0$. Thus, from Eq. 3.105-c $F'(\theta) = 0$, or $g_1'(-\pi) = g_2'(\pi)$ or

$$A = 3B = b \tag{3.118}$$

91 From those two equations we rewrite Eq. 3.116

$$g(\theta) = a\left(\sin\frac{\theta}{2} + \sin\frac{3\theta}{2}\right) + b\left(3\cos\frac{\theta}{2} + \cos\frac{3\theta}{2}\right) \tag{3.119}$$

92 We now determine the derivatives

$$\begin{aligned}f'(\theta) &= \lambda_j\sinh\lambda_j\theta && \text{(3.120-a)}\\ g'(\theta) &= a\left(\frac{3}{2}\cos\frac{3\theta}{2} + \frac{1}{2}\cos\frac{\theta}{2}\right) + b\left(-\frac{3}{2}\sin\frac{3\theta}{2} - \frac{3}{2}\sin\frac{\theta}{2}\right) && \text{(3.120-b)}\end{aligned}$$

93 Thus, we now can determine

$$\begin{aligned}F'(\theta) &= f'(\theta)g(\theta) + f(\theta)g'(\theta) && \text{(3.121-a)}\\ &= a\left\{\cosh\lambda_j\theta\left[\frac{3}{2}\cos\frac{3\theta}{2} + \frac{1}{2}\cos\frac{\theta}{2}\right] + \lambda_j\sinh\lambda_j\theta\left[\sin\frac{3\theta}{2} + \sin\frac{\theta}{2}\right]\right\}\\ &\quad +b\left\{\cosh\lambda_j\theta\left[-\frac{3}{2}\sin\frac{3\theta}{2} - \frac{3}{2}\sin\frac{\theta}{2}\right] + \lambda_j\sinh\lambda_j\theta\left[\cos\frac{3\theta}{2} + 3\cos\frac{\theta}{2}\right]\right\} && \text{(3.121-b)}\end{aligned}$$

98 where s_1 and s_2 are roots, in general complex, of Eq. 2.127 where $s_j = \alpha_j + i\beta_j$ for $j = 1, 2$, and the roots of interests are taken such that $\beta_j > 0$, and

$$p_j = a_{11}s_j^2 + a_{12} - a_{16}s_j \tag{3.125}$$

$$q_j = a_{12}s_j + \frac{a_{22}}{s_j} - a_{26} \tag{3.126}$$

99 After appropriate substitution, it can be shown that the cartesian stresses at the tip of the crack for symmetric loading are

$$\sigma_x = \frac{K_{\text{I}}}{\sqrt{2\pi r}}\text{Re}\left[\frac{s_1 s_2}{s_1 - s_2}\left(\frac{s_2}{(\cos\theta + s_2\sin\theta)^{\frac{1}{2}}} - \frac{s_1}{(\cos\theta + s_1\sin\theta)^{\frac{1}{2}}}\right)\right] \tag{3.127-a}$$

$$\sigma_y = \frac{K_{\text{I}}}{\sqrt{2\pi r}}\text{Re}\left[\frac{1}{s_1 - s_2}\left(\frac{s_1}{(\cos\theta + s_2\sin\theta)^{\frac{1}{2}}} - \frac{s_2}{(\cos\theta + s_1\sin\theta)^{\frac{1}{2}}}\right)\right] \tag{3.127-b}$$

$$\sigma_{xy} = \frac{K_{\text{I}}}{\sqrt{2\pi r}}\text{Re}\left[\frac{s_1 s_2}{s_1 - s_2}\left(\frac{1}{(\cos\theta + s_1\sin\theta)^{\frac{1}{2}}} - \frac{s_1}{(\cos\theta + s_2\sin\theta)^{\frac{1}{2}}}\right)\right] \tag{3.127-c}$$

100 and, for plane skew-symmetric loading:

$$\sigma_x = \frac{K_{\text{II}}}{\sqrt{2\pi r}}\text{Re}\left[\frac{1}{s_1 - s_2}\left(\frac{s_2^2}{(\cos\theta + s_2\sin\theta)^{\frac{1}{2}}} - \frac{s_1^2}{(\cos\theta + s_1\sin\theta)^{\frac{1}{2}}}\right)\right] \tag{3.128-a}$$

$$\sigma_y = \frac{K_{\text{II}}}{\sqrt{2\pi r}}\text{Re}\left[\frac{1}{s_1 - s_2}\left(\frac{1}{(\cos\theta + s_2\sin\theta)^{\frac{1}{2}}} - \frac{1}{(\cos\theta + s_1\sin\theta)^{\frac{1}{2}}}\right)\right] \tag{3.128-b}$$

$$\sigma_{xy} = \frac{K_{\text{II}}}{\sqrt{2\pi r}}\text{Re}\left[\frac{1}{s_1 - s_2}\left(\frac{s_1}{(\cos\theta + s_1\sin\theta)^{\frac{1}{2}}} - \frac{s_2}{(\cos\theta + s_2\sin\theta)^{\frac{1}{2}}}\right)\right] \tag{3.128-c}$$

101 For in-plane loadings, these stresses can be summed to give the stresses at a distance r and an angle θ from the crack tip.

102 An important observation to be made is that the form of the stress singularity $r^{-1/2}$ is identical to the one found in isotropic solids.

103 It should be noted that contrarily to the isotropic case where both the stress magnitude and its spatial distribution are controlled by the stress intensity factor only, in the anisotropic case they will also depend on the material elastic properties and the orientation of the crack with respect to the principal planes of elastic symmetry (through s_1 and s_2).

3.8 Assignment

CVEN-6831

FRACTURE MECHANICS

3. The stress intensity factor of the following problem:

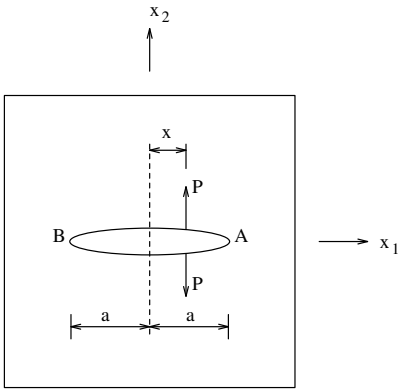

is given by:

$$K_A = \frac{P}{\sqrt{\pi a}}\sqrt{\frac{a+x}{a-x}} \tag{3.130}$$

$$K_b = \frac{P}{\sqrt{\pi a}}\sqrt{\frac{a-x}{a+x}} \tag{3.131}$$

Based on those expressions, and results from the previous problem, determine the stress function Φ.

4. Barenblatt's model assumes a linearly varying closing pressure at the tip of a crack,

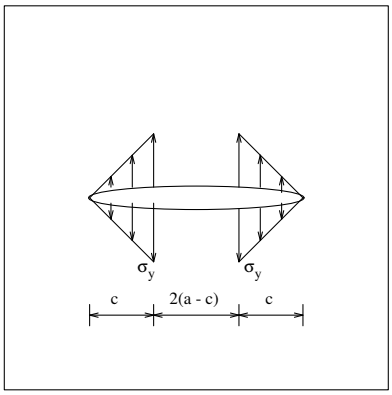

Using Mathematica and the expressions of K_A and K_B from the previous problem, determine an expression for the stress intensity factors for this case.

5. Using Mathematica, program either:

   (a) Westergaard's solution for a crack subjected to mode I and mode II loading.

   (b) Williams solution for a crack along dissimilar materials.

Chapter 4

LEFM DESIGN EXAMPLES

1 Following the detailed coverage of the derivation of the linear elastic stress field around a crack tip, and the introduction of the concept of a stress intensity factor in the preceding chapter, we now seek to apply those equations to some (pure mode I) practical design problems.

2 First we shall examine how is linear elastic fracture mechanics (LEFM) effectively used in design examples, then we shall give analytical solutions to some simple commonly used test geometries, followed by a tabulation of fracture toughness of commonly used engineering materials. Finally, this chapter will conclude with some simple design/analysis examples.

4.1 Design Philosophy Based on Linear Elastic Fracture Mechanics

3 One of the underlying principles of fracture mechanics is that *unstable* fracture occurs when the stress intensity factor (SIF) reaches a critical value K_{Ic}, also called *fracture toughness*. K_{Ic} represents the inherent ability of a material to withstand a given stress field intensity at the tip of a crack and to resist progressive tensile crack extension.

4 Thus a crack will propagate (under pure mode I), whenever the stress intensity factor K_I (which characterizes the strength of the singularity for a given problem) reaches a material constant K_{Ic}. Hence, under the assumptions of linear elastic fracture mechanics (LEFM), at the point of incipient crack growth:

$$K_{Ic} = \beta\sigma\sqrt{\pi a} \tag{4.1}$$

5 Thus for the design of a cracked, or potentially cracked, structure, the engineer would have to decide what design variables can be selected, as only, two of these variables can be fixed, and the third must be determined. The design variables are:

Material properties: (such as special steel to resist corrosive liquid) $\Rightarrow K_c$ is fixed.

Design stress level: (which may be governed by weight considerations) $\Rightarrow \sigma$ is fixed.

Flaw size: [1], a.

[1] In most cases, a refers to half the total crack length.

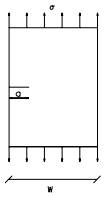

Figure 4.2: Single Edge Notch Tension Panel

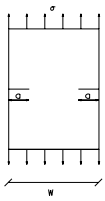

Figure 4.3: Double Edge Notch Tension Panel

Single Edge Notch Tension Panel (SENT) for $\frac{L}{W} = 2$, Fig. 4.2

$$K_I = \underbrace{\left[1.12 - 0.23\left(\frac{a}{W}\right) + 10.56\left(\frac{a}{W}\right)^2 - 21.74\left(\frac{a}{W}\right)^3 + 30.42\left(\frac{a}{W}\right)^4\right]}_{\beta} \sigma\sqrt{\pi a} \tag{4.4}$$

We observe that here the β factor for small crack ($\frac{a}{W} \ll 1$) is grater than one and is approximately 1.12.

Double Edge Notch Tension Panel (DENT), Fig. 4.3

$$K_I = \underbrace{\left[1.12 + 0.43\left(\frac{a}{W}\right) - 4.79\left(\frac{a}{W}\right)^2 + 15.46\left(\frac{a}{W}\right)^3\right]}_{\beta} \sigma\sqrt{\pi a} \tag{4.5}$$

Three Point Bend (TPB), Fig. 4.4

$$K_I = \frac{3\sqrt{\frac{a}{W}}\left[1.99 - \left(\frac{a}{W}\right)\left(1 - \frac{a}{W}\right)\left(2.15 - 3.93\frac{a}{W} + 2.7\left(\frac{a}{W}\right)^2\right)\right]}{2\left(1 + 2\frac{a}{W}\right)\left(1 - \frac{a}{W}\right)^{\frac{3}{2}}} \frac{PS}{BW^{\frac{3}{2}}} \tag{4.6}$$

Compact Tension Specimen (CTS), Fig. 4.5 used in ASTM E-399 (399 n.d.) Standard Test Method for Plane-Strain Fracture Toughness of Metallic Materials

$$K_I = \underbrace{\left[16.7 - 104.6\left(\frac{a}{W}\right) + 370\left(\frac{a}{W}\right)^2 - 574\left(\frac{a}{W}\right)^3 + 361\left(\frac{a}{W}\right)^4\right]}_{\beta} \underbrace{\frac{P}{BW}}_{\sigma} \sqrt{\pi a} \tag{4.7}$$

We note that this is not exactly the equation found in the ASTM standard, but rather an equivalent one written in the standard form.

Chapter 5

THEORETICAL STRENGTH of SOLIDS; (Griffith I)

1 We recall that Griffith's involvement with fracture mechanics started as he was exploring the disparity in strength between glass rods of different sizes, (Griffith 1921). As such, he had postulated that this can be explained by the presence of internal flaws (idealized as elliptical) and then used Inglis solution to explain this discrepancy.

2 In this section, we shall develop an expression for the theoretical strength of perfect crystals (theoretically the strongest form of solid). This derivation, (Kelly 1974) is fundamentally different than the one of Griffith as it starts at the atomic level.

5.1 Derivation

3 We start by exploring the energy of interaction between two adjacent atoms at equilibrium separated by a distance a_0, Fig. 5.1. The total energy which must be supplied to separate atom C from C' is

$$U_0 = 2\gamma \tag{5.1}$$

where γ is the surface energy[1], and the factor of 2 is due to the fact that upon separation, we have two distinct surfaces.

5.1.1 Tensile Strength

5.1.1.1 Ideal Strength in Terms of Physical Parameters

We shall first derive an expression for the ideal strength in terms of physical parameters, and in the next section the strength will be expressed in terms of engineering ones.

[1] From watching raindrops and bubbles it is obvious that liquid water has surface tension. When the surface of a liquid is extended (soap bubble, insect walking on liquid) work is done against this tension, and energy is stored in the new surface. When insects walk on water it sinks until the surface energy just balances the decrease in its potential energy. For solids, the chemical bonds are stronger than for liquids, hence the surface energy is stronger. The reason why we do not notice it is that solids are too rigid to be distorted by it. Surface energy γ is expressed in J/m^2 and the surface energies of water, most solids, and diamonds are approximately .077, 1.0, and 5.14 respectively.

Chapter 6

ENERGY TRANSFER in CRACK GROWTH; (Griffith II)

1 In the preceding chapters, we have focused on the singular stress field around a crack tip. On this basis, a criteria for crack propagation, based on the strength of the singularity was first developed and then used in practical problems.

2 An alternative to this approach, is one based on energy transfer (or release), which occurs during crack propagation. This dual approach will be developed in this chapter.

3 Griffith's main achievement, in providing a basis for the fracture strengths of bodies containing cracks, was his realization that it was possible to derive a thermodynamic criterion for fracture by considering the total change in energy of a cracked body as the crack length increases, (Griffith 1921).

4 Hence, Griffith showed that material fail not because of a maximum stress, but rather because a certain energy criteria was met.

5 Thus, the Griffith model for elastic solids, and the subsequent one by Irwin and Orowan for elastic-plastic solids, show that crack propagation is caused by a transfer of energy transfer from external work and/or strain energy to surface energy.

6 It should be noted that this is a *global energy* approach, which was developed prior to the one of Westergaard which focused on the stress field surrounding a crack tip. It will be shown later that for linear elastic solids the two approaches are identical.

6.1 Thermodynamics of Crack Growth

6.1.1 General Derivation

7 If we consider a crack in a deformable continuum subjected to arbitrary loading, then the first law of thermodynamics gives: The change in energy is proportional to the amount of work performed. Since only the change of energy is involved, any datum can be used as a basis for measure of energy. Hence energy is neither created nor consumed.

8 The first law of thermodynamics states *The time-rate of change of the total energy (i.e., sum of the kinetic energy and the internal energy) is equal to the sum of the rate of work done by*

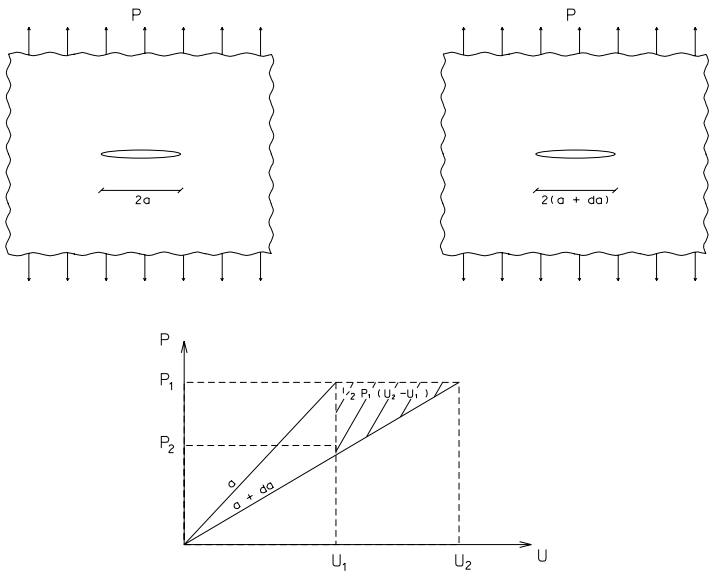

Figure 6.1: Energy Transfer in a Cracked Plate

length $2a$ located in an infinite plate subjected to load P. Griffith assumed that it was possible to produce a macroscopical load displacement $(P-u)$ curve for two different crack lengths a and $a+\mathrm{d}a$.

Two different boundary conditions will be considered, and in each one the change in potential energy as the crack extends from a to $a+\mathrm{d}a$ will be determined:

Fixed Grip: $(u_2 = u_1)$ loading, an increase in crack length from a to $a+\mathrm{d}a$ results in a decrease in stored elastic strain energy, ΔU,

$$\begin{aligned} \Delta U &= \frac{1}{2}P_2u_1 - \frac{1}{2}P_1u_1 && (6.6)\\ &= \frac{1}{2}\left(P_2 - P_1\right)u_1 && (6.7)\\ &< 0 && (6.8) \end{aligned}$$

Furthermore, under fixed grip there is no external work $(u_2 = u_1)$, so the decrease in potential energy is the same as the decrease in stored internal strain energy, hence

$$\begin{aligned} \Pi_2 - \Pi_1 &= \Delta W - \Delta U && (6.9)\\ &= -\frac{1}{2}(P_2 - P_1)u_1 = \frac{1}{2}(P_1 - P_2)u_1 && (6.10) \end{aligned}$$

Fixed Load: $P_2 = P_1$ the situation is slightly more complicated. Here there is both external work

$$\Delta W = P_1(u_2 - u_1) \tag{6.11}$$

and a release of internal strain energy. Thus the net effect is a change in potential energy given by:

$$\Pi_2 - \Pi_1 = \Delta W - \Delta U \tag{6.12}$$

Chapter 7

MIXED MODE CRACK PROPAGATION

1 Practical engineering cracked structures are subjected to mixed mode loading, thus in general K_I and K_{II} are both nonzero, yet we usually measure only mode I fracture toughness K_{Ic} (K_{IIc} concept is seldom used). Thus, so far the only fracture propagation criterion we have is for mode I only (K_I vs K_{Ic}, and G_I vs R).

2 Whereas under pure mode I in homogeneous isotropic material, crack propagation is collinear, in all other cases the propagation will be curvilinear and at an angle θ_0 with respect to the crack axis. Thus, for the general mixed mode case, we seek to formulate a criterion that will determine:

1. The angle of incipient propagation, θ_0, with respect to the crack axis.
2. If the stress intensity factors are in such a critical combination as to render the crack locally unstable and force it to propagate.

3 Once again, for pure mode I problems, fracture initiation occurs if:

$$K_{\mathrm{I}} \geq K_{\mathrm{Ic}} \tag{7.1}$$

4 The determination of a fracture initiation criterion for an existing crack in mode I and II would require a relationship between $K_{\mathrm{I}}, K_{\mathrm{II}}$, and K_{Ic} of the form

$$F\left(K_{\mathrm{I}}, K_{\mathrm{II}}, K_{\mathrm{Ic}}\right) = 0 \tag{7.2}$$

and would be analogous to the one between the two principal stresses and a yield stress, Fig. 7.1

$$F_{yld}(\sigma_1, \sigma_2, \sigma_y) = 0 \tag{7.3}$$

Such an equation may be the familiar von Mises criterion.

5 In the absence of a widely accepted criterion for mixed mode crack growth, three of the most widely used criterion are discussed below.

Solution of the second equation yields the angle of crack extension θ_0

$$\boxed{\tan\frac{\theta_0}{2} = \frac{1}{4}\frac{K_{\mathrm{I}}}{K_{\mathrm{II}}} \pm \frac{1}{4}\sqrt{\left(\frac{K_{\mathrm{I}}}{K_{\mathrm{II}}}\right)^2 + 8}} \tag{7.8}$$

10 For the crack to extend, the maximum circumferential tensile stress, σ_θ (from Eq. 3.55-b and 3.56-b)

$$\sigma_\theta = \frac{K_{\mathrm{I}}}{\sqrt{2\pi r}}\cos\frac{\theta_0}{2}\left(1-\sin^2\frac{\theta_0}{2}\right) + \frac{K_{\mathrm{II}}}{\sqrt{2\pi r}}\left(-\frac{3}{4}\sin\frac{\theta_0}{2} - \frac{3}{4}\sin\frac{3\theta_0}{2}\right) \tag{7.9}$$

must reach a critical value which is obtained by rearranging the previous equation

$$\sigma_{\theta max}\sqrt{2\pi r} = K_{\mathrm{Ic}} = \cos\frac{\theta_0}{2}\left[K_{\mathrm{I}}\cos^2\frac{\theta_0}{2} - \frac{3}{2}K_{\mathrm{II}}\sin\theta_0\right] \tag{7.10}$$

which can be normalized as

$$\boxed{\frac{K_{\mathrm{I}}}{K_{\mathrm{Ic}}}\cos^3\frac{\theta_0}{2} - \frac{3}{2}\frac{K_{\mathrm{II}}}{K_{\mathrm{Ic}}}\cos\frac{\theta_0}{2}\sin\theta_0 = 1} \tag{7.11}$$

11 This equation can be used to define an equivalent stress intensity factor K_{eq} for mixed mode problems

$$\boxed{K_{eq} = K_{\mathrm{I}}\cos^3\frac{\theta_0}{2} - \frac{3}{2}K_{\mathrm{II}}\cos\frac{\theta_0}{2}\sin\theta_0} \tag{7.12}$$

7.1.2 Maximum Energy Release Rate

12 In their original model, Erdogan, F. and Sih, G.C. (1963) noted that:

> "If we accept Griffith (energy) theory as the valid criteria which explains crack growth, then the crack will grow in the direction along which the elastic energy release per unit crack extension will be maximum and the crack will start to grow when this energy reaches a critical value (or $G = G(\delta,\ \theta)$). Evaluation of $G(\delta,\ \theta)$ poses insurmountable mathematical difficulties."

13 Finding $G(\delta,\ \theta)$ will establish for the general mixed mode case the duality which is the basis of fracture mechanics: the equivalence in viewing fracture initiation from either a global energy balance or a local stress intensity point of view.

14 This (insurmountable) problem was solved in 1974, by Hussain et al. (1974). Fundamentally, Hussain et al. (1974) have solved for the stress intensity factor of a major crack with an infinitesimal "kink" at an angle θ, $K_I(\theta)$ and $K_{II}(\theta)$ in terms of the stress intensity factors of the original crack K_I and K_{II}, Fig. 7.2:

$$\begin{Bmatrix} K_I(\theta) \\ K_{II}(\theta) \end{Bmatrix} = \left(\frac{4}{3+\cos^2\theta}\right)\left(\frac{1-\frac{\theta}{\pi}}{1+\frac{\theta}{\pi}}\right)^{\frac{\theta}{2\pi}} \begin{Bmatrix} K_I\cos\theta + \frac{3}{2}K_{II}\sin\theta \\ K_{II}\cos\theta - \frac{1}{2}K_I\sin\theta \end{Bmatrix} \tag{7.13}$$

Part II

ELASTO PLASTIC FRACTURE MECHANICS

Chapter 8

PLASTIC ZONE SIZES

1 it was shown in chapter **??** that, under linear elastic fracture mechanics assumptions, the stress at the crack tip is theoretically infinite. Clearly, all materials have a finite strength, thus there will always be a small plastified zone around the crack tip.

2 If this zone is small compared to the crack size, then our linear elastic assumptions are correct; if not, LEFM is not applicable (thus it would be incorrect to use a K or G criterion) and a nonlinear model must be used. This "damaged" zone is referred to as a *plastic zone* for metals, and a *fracture process zone* for cementitious materials and ceramics.

3 Thus there are two important issues associated with nonlinear fracture:

1. What is the size of the plastic or process zone?
2. What are the criteria for crack growth?

4 This chapter will answer the first question by focusing on metals[1], whereas the next chapter will develop criterions for crack growth.

5 The evaluation of the plastic zone for plastified materials can be determined through various levels of approximations:

1. Uniaxial stress criteria
   (a) first order approximation
   (b) second order approximation (Irwin)
   (c) Dugdale's model
2. Multiaxial yield criteria

Each one of them will be separately reviewed.

8.1 Uniaxial Stress Criteria

6 First we shall examine criteria in which only the uniaxial stress state (σ_{yy} normal to thee crack axis) and we shall consider three models of increasing complexities.

[1] Due to the intrinsically different behavior of concrete compared to metals, estimates of the fracture process zone will be separately discussed.

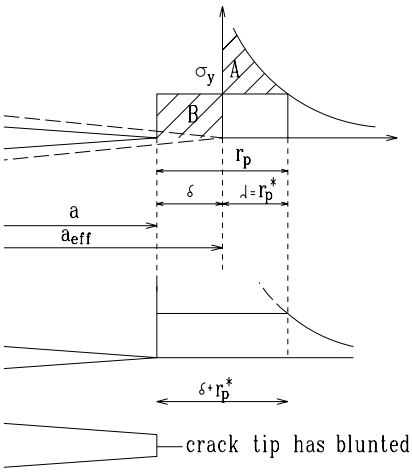

Figure 8.2: Second-Order Approximation of the Plastic Zone

$$\begin{aligned} &= \int_0^{r_p^*} \sigma\sqrt{\frac{a}{2}} r^{-\frac{1}{2}} \mathrm{d}r - \sigma_{\text{yld}} r_p^* \\ &= \sigma\sqrt{\frac{a}{2}} 2r^{\frac{1}{2}} \Big|_0^{r_p^*} - \sigma_{\text{yld}} r_p^* \\ &= \sigma\sqrt{2ar_p^*} - \sigma_{\text{yld}} r_p^* \end{aligned} \tag{8.5}$$

9 Equating A to B we obtain:

$$\begin{aligned} \sigma\sqrt{2ar_p^*} - \sigma_{\text{yld}} r_p^* &= \sigma_{\text{yld}}\delta \\ \sigma_{\text{yld}}(\delta + r_p^*) &= \sigma\sqrt{2ar_p^*} \\ (\delta + r_p^*)^2 &= \frac{2a\sigma^2}{\sigma_{\text{yld}}^2} r_p^* \end{aligned} \tag{8.6}$$

10 From Eq. 8.3, $r_p^* = \frac{a}{2}\left(\frac{\sigma}{\sigma_{\text{yld}}}\right)^2$, thus this simplifies into

$$\delta + r_p^* = 2r_p^* \Rightarrow \delta = r_p^* \tag{8.7}$$

$$r_p = 2r_p^* \tag{8.8}$$

$$\boxed{r_p = \frac{1}{\pi}\frac{K_I}{\sigma_{\text{yld}}^2} = \left(\frac{\sigma}{\sigma_{\text{yld}}}\right)^2 a} \tag{8.9}$$

11 Note that $r_p = 2r_p^*$ and that we can still use r_p^* but with $a_{eff} = a + r_p^*$; thus we can consider an effective crack length of $a + r_p^*$ which would result in:

$$\boxed{K_{eff} = f(g)\sigma\sqrt{\pi(a + r_p^*)} = f(g)\sigma\sqrt{\pi(a + \frac{K^2}{2\pi\sigma_{\text{yld}}^2})}} \tag{8.10}$$

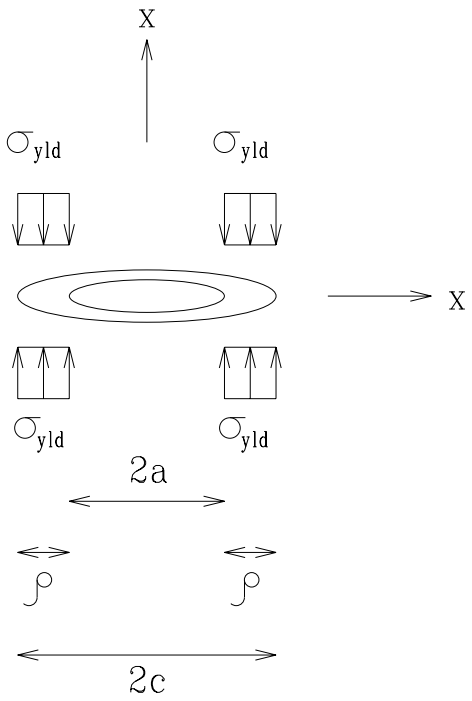

Figure 8.3: Dugdale's Model

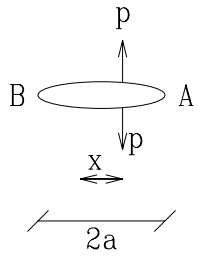

Figure 8.4: Point Load on a Crack

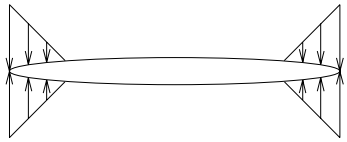

Figure 8.6: Barenblatt's Model

8.2 Multiaxial Yield Criteria

24 All the previous models have restricted themselves to $\theta = 0$ and have used uniaxial yield criteria, but the size of the plastic zone can be similarly derived from a multi-axial yield criterion.

25 The principal stresses at a point with respect to the crack tip are given by:

$$\sigma_{1,2} = \frac{\sigma_x + \sigma_y}{2} \pm \sqrt{\left(\frac{\sigma_x - \sigma_y}{2}\right)^2 + \tau_{xy}^2} \tag{8.24}$$

where the stresses were obtained in Eq. 3.52-a, 3.52-b, and 3.52-c

$$\sigma_1 = \frac{K_\mathrm{I}}{\sqrt{2\pi r}} \cos\frac{\theta}{2}\left[1 + \sin\frac{\theta}{2}\right] \tag{8.25}$$

$$\sigma_2 = \frac{K_\mathrm{I}}{\sqrt{2\pi r}} \cos\frac{\theta}{2}\left[1 - \sin\frac{\theta}{2}\right] \tag{8.26}$$

$$\sigma_3 = \nu(\sigma_1 + \sigma_2) \tag{8.27}$$

for plane strain, or

$$\sigma_3 = 0 \tag{8.28}$$

for plane stress.

26 With those stress expressions, any yield criteria could be used. Using the von Mises criteria, we would obtain:

$$\sigma_e = \frac{1}{\sqrt{2}}\left[(\sigma_1 - \sigma_2)^2 + (\sigma_2 - \sigma_3)^2 + (\sigma_3 - \sigma_1)^2\right]^{\frac{1}{2}} \tag{8.29}$$

and yielding would occur when σ_e reaches σ_{yld}. Substituting the principal stresses (with $r = r_p$) into this equation and solving for r_p yields

- For plane strain:

$$r_p(\theta) = \frac{1}{4\pi}\frac{K_I}{\sigma_{\text{yld}}^2}\left[\frac{3}{2}\sin^2\theta + (1-2\nu)^2(1+\cos\theta)\right] \tag{8.30}$$

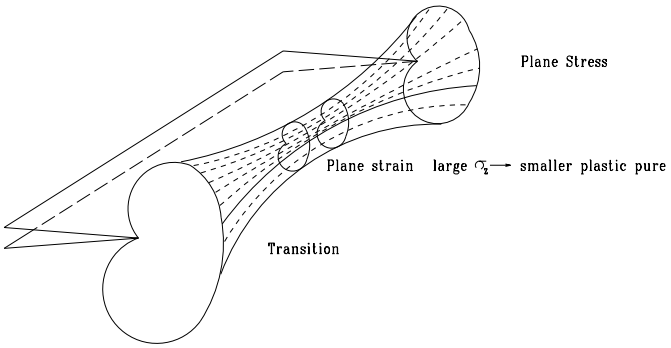

Figure 8.8: Plastic Zone Size Across Plate Thickness

31 We also observe that since r_p is proportional to $\left(\frac{K_I}{\sigma_{\text{yld}}}\right)^2$, the plate thickness should increase as either the SIF increase or the yield stress decrease.

32 Furthermore, the different stress fields present at the tip of the crack under plane stress and plane strain will result in different deformation patterns. This is best explained in terms of the orientation of the planes of maximum shear stress for both cases, Fig. 8.9.

Plane Stress: $\sigma_z = 0$, and the maximum shear stress τ_{max} is equal to $\frac{\sigma_x}{2}$ and occurs at approximately 45 degrees from the crack plane.

Plane Strain: In this case we have $\sigma_y < \sigma_z < \sigma_x$, and the maximum shear stress is equal to $\frac{\sigma_x - \sigma_y}{2}$ which is not only much smaller than $\frac{\sigma_x}{2}$ but occurs on different planes.

33 Finally, it should be noted, once again, that fracture toughness K_{Ic} can only be measured under plane strain conditions, Fig. 8.10

Chapter 9

FATIGUE CRACK PROPAGATION

1 When a subcritical crack (a crack whose stress intensity factor is below the critical value) is subjected to either repeated or fatigue load, or is subjected to a corrosive environment, crack propagation will occur.

2 As in many structures one has to assume the presence of minute flaws (as large as the smallest one which can be detected). The application of repeated loading will cause crack growth. The loading is usually caused by vibrations.

3 Thus an important question that arises is "how long would it be before this subcritical crack grows to reach a critical size that would trigger failure?" To predict the minimum fatigue life of metallic structures, and to establish safe inspection intervals, an understanding of the rate of fatigue crack propagation is required.

Historically, fatigue life prediction was based on $S - N$ curves, Fig. 9.1 (or Goodman's

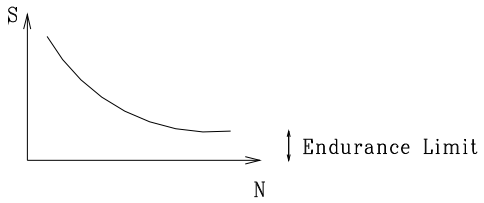

Figure 9.1: S-N Curve and Endurance Limit

Diagram) using a Strength of Material Approach which did NOT assume the presence of a crack.

9.1 Experimental Observation

4 If we start with a plate that has no crack and subject it to a series of repeated loading, Fig. 9.2 between σ_{min} and σ_{max}, we would observe three distinct stages, Fig. 9.3

1. Stage 1 : Micro coalescence of voids and formation of microcracks. This stage is difficult to capture and is most appropriately investigated by metallurgists or material scientists,

law based on experimental observations. Most other empirical fatigue laws can be considered as direct extensions, or refinements of this one, given by

$$\boxed{\frac{\mathrm{d}a}{\mathrm{d}N} = C\,(\Delta K)^n} \tag{9.1}$$

which is a straight line on a log-log plot of $\frac{\mathrm{d}a}{\mathrm{d}N}$ vs ΔK, and

$$\Delta K = K_{max} - K_{min} = (\sigma_{max} - \sigma_{min}) f(g) \sqrt{\pi a} \tag{9.2}$$

a is the crack length; N the number of load cycles; C the intercept of line along $\frac{\mathrm{d}a}{\mathrm{d}N}$ and is of the order of 10^{-6} and has units of length/cycle; and n is the slope of the line and ranges from 2 to 10.

10 Equation 9.1 can be rewritten as :

$$\Delta N = \frac{\Delta a}{C\,[\Delta K(a)]^n} \tag{9.3}$$

or

$$\boxed{N = \int \mathrm{d}N = \int_{a_i}^{a_f} \frac{\mathrm{d}a}{C\,[\Delta K(a)]^n}} \tag{9.4}$$

11 Thus it is apparent that a small error in the SIF calculations would be magnified greatly as n ranges from 2 to 6. Because of the sensitivity of N upon ΔK, it is essential to properly determine the numerical values of the stress intensity factors.

12 However, in most practical cases, the crack shape, boundary conditions, and load are in such a combination that an analytical solution for the SIF does not exist and large approximation errors have to be accepted. Unfortunately, analytical expressions for K are available for only few simple cases. Thus the stress analyst has to use handbook formulas for them (Tada et al. 1973). A remedy to this problem is the usage of numerical methods, of which the finite element method has achieved greatest success.

9.2.2 Foreman's Model

13 When compared with experimental data, it is evident that Paris law does not account for:

1. Increase in crack growth rate as K_{max} approaches K_{Ic}
2. Slow increase in crack growth at $K_{min} \approx K_{th}$

thus it was modified by Foreman (Foreman, Kearney and Engle 1967), Fig. 9.4

$$\frac{\mathrm{d}a}{\mathrm{d}N} = \frac{C(\Delta K)^n}{(1-R)K_c - \Delta K} \tag{9.5}$$

9.2.3 Modified Walker's Model

14 Walker's (Walker 1970) model is yet another variation of Paris Law which accounts for the stress ratio $R = \frac{K_{min}}{K_{max}} = \frac{\sigma_{min}}{\sigma_{max}}$

$$\frac{\mathrm{d}a}{\mathrm{d}N} = C\left[\frac{\Delta K}{(1-R)^{(1-m)}}\right]^n \tag{9.6}$$

aluminum which has $R = 15$ kJ/m^2 $E = 70$ GPa $C = 5 \times 10^{-11}$ m/cycle, and $n = 3$. The smallest detectable flaw is 4 mm. How long would it be before the crack will propagate to its critical length?

Assuming $K = \sigma\sqrt{\pi a}$ and $K_c = \sqrt{ER}$, then $a_c = \frac{K_c^2}{\sigma_{max}^2 \pi} = \frac{ER}{\sigma_{max}^2 \pi}$ or

$$a_c = \frac{(70 \times 10^9)(15 \times 10^3)}{(200 \times 10^6)^2 \pi} = 0.0084m = 8.4mm \tag{9.8}$$

$$\begin{aligned} \Rightarrow N &= \int_{a_i}^{a_f} \frac{\mathrm{d}a}{C[\Delta K(a)]^n} = \int_{a_i}^{a_f} \frac{\mathrm{d}a}{C \underbrace{(\sigma_{max} - \sigma_{min})^n}_{(\Delta\sigma)^n} ((\pi a)^{\frac{1}{2}})^n} \\ &= \int_{4\times10^{-3}}^{8.4\times10^{-3}} \frac{\mathrm{d}a}{\underbrace{(5 \times 10^{-11})}_{C} \underbrace{(200-50)^3}_{(\Delta\sigma)^3} \underbrace{(\pi a)^{1.5}}_{((\pi a)^{\cdot 5})^3}} = 1064 \int_{.004}^{.0084} a^{-1.5} \mathrm{d}a \\ &= -2128 a^{-.5} \,|_{.004}^{.0084} = 2128[-\tfrac{1}{\sqrt{.0084}} + \tfrac{1}{\sqrt{.004}}] \\ &= 10,428 \text{ cycles} \end{aligned} \tag{9.9}$$

thus the time t will be: t = (10,428) cycles $\times \frac{1}{10} \frac{\text{flight}}{\text{cycle}} \times \frac{1}{2} \frac{\text{day}}{\text{flight}} \times \frac{1}{30} \frac{\text{month}}{\text{day}} \approx 17.38$ month ≈ 1.5 years.

If a longer lifetime is desired, then we can:

1. Employ a different material with higher K_{Ic}, so as to increase the critical crack length a_c at instability.
2. Reduce the maximum value of the stress σ_{max}.
3. Reduce the stress range $\Delta\sigma$.
4. Improve the inspection so as to reduce the assumed initial crack length a_{min}.

9.2.6.2 Example 2

21 Repeat the previous problem except that more sophisticated (and expensive) NDT equipment is available with a resolution of .1 mm thus $a_i = .1$mm

$t = 2128[-\frac{1}{\sqrt{.0084}} + \frac{1}{\sqrt{.0001}}] = 184,583$ cycles

$t = \frac{1738}{10,428}(189,583) = 316$ months ≈ 26 years!

9.2.6.3 Example 3

Rolfe and Barsoum p.261-263.

9.3 Variable Amplitude Loading

9.3.1 No Load Interaction

22 Most Engineering structures are subjected to variable amplitude repeated loading, however, most experimental data is based on constant amplitude load test. Thus, the following questions arise:

Chapter 10

CRACK TIP OPENING DISPLACEMENTS

1 Within the assumptions and limitations of LEFM we have two valid (and equivalent) criteria for crack propagation: 1) K vs K_{Ic} which is a local criteria based on the strength of the stress singularity at the tip of the crack; and 2) G vs G_{Ic} (or R) which is a global criteria based on the amount of energy released (or consumed) during a unit surface crack's propagations.

2 In many cases it is found that LEFM based criteria is either: too conservative and expensive as it does not account for plastification at the crack tip, and/or invalid based on calculations of r_p^* where LEFM assumptions are checked.

3 Thus, in those cases where LEFM is not applicable, an alternative criteria for crack growth in Elasto Plastic Fracture Mechanics (EPFM) is sought.

4 But first let us note the various stages of ductile fracture:

1. Blunting of an initially sharp crack. Under LEFM assumptions, the crack tip opening displacement (CTOD) is zero, however in elasto-plastic material due to blunting it is different from zero, Fig. 10.1.

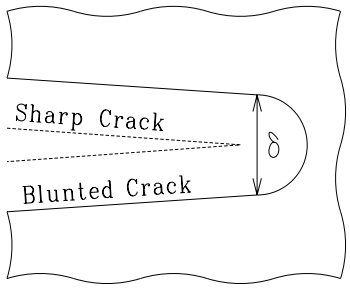

Figure 10.1: Crack Tip Opening Displacement, (Anderson 1995)

2. Crack initiation
3. Slow (stable) crack growth
4. Unstable crack growth

$$v = \frac{K_{\mathrm{I}}}{2\mu}\left[\frac{r}{2\pi}\right]^{\frac{1}{2}} \sin\frac{\theta}{2}\left[\kappa + 1 - 2\cos^2\frac{\theta}{2}\right] \tag{10.1}$$

11 If we substitute $\theta = \pm\pi$ we obtain the upper and lower displacements of the crack face, and due to symmetry their sum corresponds to the crack opening displacement. Hence the crack opening is given by

$$\mathrm{COD} = 2v = \frac{\kappa+1}{\mu} K_I \sqrt{\frac{r}{2\pi}} \tag{10.2}$$

12 If we determine the crack tip opening displacement a distance r_p^* away from the crack tip using Irwin's plastic zone correction from Eq. 8.9

$$r_p^* = \frac{1}{2\pi}\frac{K_I^2}{\sigma_{\mathrm{yld}}^2} \tag{10.3}$$

and using $\kappa = \frac{3-\nu}{1+\nu}$ for plane stress we obtain

$$\boxed{\mathrm{CTOD} = \frac{4}{\pi}\frac{K_I^2}{E\sigma_{\mathrm{yld}}}} \tag{10.4}$$

10.1.2 Dugdale's Solution

13 Using Dugdale's solution, Kanninen (Kanninen 1984) has shown that the crack opening along the crack is given by[1]:

$$v(x) = \frac{2}{\pi}\frac{a\sigma_{\mathrm{yld}}}{E}\left\{\log\left|\frac{\sqrt{c^2-a^2}+\sqrt{c^2-x^2}}{\sqrt{c^2-a^2}-\sqrt{c^2-x^2}}\right| + \frac{x}{a}\log\left|\frac{x\sqrt{c^2-a^2}+a\sqrt{c^2-x^2}}{x\sqrt{c^2-a^2}-a\sqrt{c^2-x^2}}\right|\right\} \tag{10.5}$$

for $0 \le x \le c$. For $x = a$ this reduces to

$$v(a) = \frac{4}{\pi}\frac{a\sigma_{\mathrm{yld}}}{E}\log\frac{c}{a} \tag{10.6}$$

14 Combining this equation with Dugdale's solution for c from Eq. 8.21,

$$\frac{a}{c} = \cos\frac{\pi}{2}\frac{\sigma}{\sigma_{\mathrm{yld}}} \tag{10.7}$$

we would then obtain

$$\mathrm{CTOD} = 2v = \frac{8}{\pi}\frac{a\sigma_{\mathrm{yld}}}{E}\log\left[\sec\frac{\pi}{2}\frac{\sigma}{\sigma_{\mathrm{yld}}}\right] \tag{10.8}$$

15 using the series expansion of $\log\sec$:

$$\mathrm{CTOD} = \frac{8}{\pi}\frac{a\sigma_{\mathrm{yld}}}{E}\left[\frac{1}{2}\left(\frac{\pi}{2}\frac{\sigma}{\sigma_{\mathrm{yld}}}\right)^2 + \frac{1}{12}\left(\frac{\pi}{2}\frac{\sigma}{\sigma_{\mathrm{yld}}}\right)^4 + \cdots\right] \tag{10.9}$$

or

$$\boxed{\mathrm{CTOD} = \frac{K^2}{E\sigma_{\mathrm{yld}}}\left[1 + \frac{\pi^2}{24}\frac{\sigma^2}{\sigma_{\mathrm{yld}}^2} + \ldots\right]} \tag{10.10}$$

note that for small $\frac{\sigma}{\sigma_{\mathrm{yld}}}$, the $CTOD$ can be approximated by $CTOD = \frac{K^2}{E\sigma_{\mathrm{yld}}}$.

[1] Derivation of this equation can be found on p. 203 of (Anderson 1995)

Chapter 11

J INTEGRAL

11.1 Genesis

1 Eshelby (Eshelby 1974) has defined a number of contour integrals that are path independent by virtue of the theorem of energy conservation. The two-dimensional form of one of these integrals can be written as:

$$J = \oint_{\Gamma} \left(w \mathrm{d}y - \mathbf{t} \frac{\partial \mathbf{u}}{\partial x} \mathrm{d}y \right) = 0 \tag{11.1}$$

with

$$w = \int_0^{\varepsilon} \sigma_{ij} \mathrm{d}\varepsilon_{ij} \tag{11.2}$$

where w is the strain energy density; Γ is a closed contour followed counter-clockwise, as shown in Fig. 11.1; $\mathbf{t}$ is the traction vector on a plane defined by the outward drawn normal $\mathbf{n}$ and $\mathbf{t} = \boldsymbol{\sigma}\mathbf{n}$; $\mathbf{u}$ the displacement vector, and $\mathrm{d}y$ is the element of the arc along the path Γ.

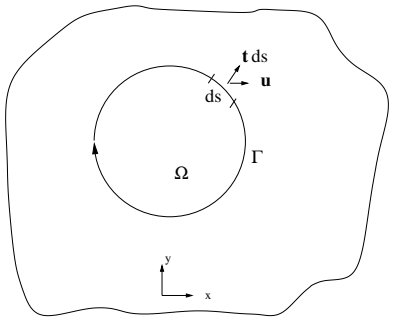

Figure 11.1: J Integral Definition Around a Crack

2 Whereas Eshelby had defined a number of similar path independent contour integrals, he had not assigned them with a particular physical meaning.

9 Thus the integrand of Eq. 11.3 vanishes and $J = 0$ for any closed contour.

10 Having shown that indeed $J = 0$, we will now exploit this to proove that around a crack, J is non-zero and is independent of the path.

11 With reference to Fig. 11.2 if we consider the closed path $\Gamma = \Gamma_1 + \Gamma_2 + \Gamma_3 + \Gamma_4$ in which Γ_1 and Γ_3 are arbitrarily chosen contours. Obviously $J = 0$ over Γ in order to satisfy compatibility conditions, provided that the stresses and displacement gradients are continuous. Along paths Γ_2 and Γ_4, the traction vector $t_i = 0$ and also $\mathrm{d}y = 0$. Consequently, the contributions to J from Γ_2 and Γ_4 vanish. Taking into account the difference sense of integration along paths Γ_1 and Γ_3 we arrive at the conclusion that the values of J integrated over paths Γ_1 and Γ_3 are identical. Because these two paths were arbitrarily chosen, the path independence of J is assured.

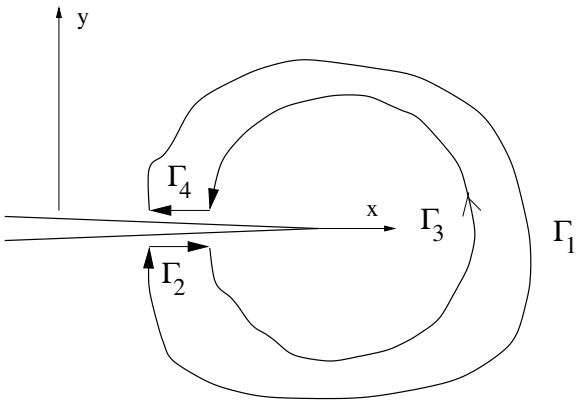

Figure 11.2: Closed Contour for Proof of J Path Independence

11.3 Nonlinear Elastic Energy Release Rate

12 Let us now establish the connection between the two previous interpretations of J, the one mathematically defined by Eshelby, and the one associated with the energy release rate (yet to be proven). We shall prove that when J is applied along a contour around a crack tip, it represents the change in potential energy for a virtual crack extension $\mathrm{d}a$. Two slightly different derivations are presented.

11.3.1 Virtual Crack Extension

13 Considering a two-dimensional crack surrounded by a line Γ which encompasses an area Ω. Under quasi-static conditions, and in the absence of body forces, the potential energy is given by

$$\Pi = \int_\Omega w \mathrm{d}\Omega - \oint_\Gamma t_i u_i \mathrm{d}y \tag{11.12}$$

14 For a virtual crack extension, the change in potential energy is

$$\frac{\mathrm{d}\Pi}{\mathrm{d}a} = \int_\Omega \frac{\mathrm{d}w}{\mathrm{d}a}\mathrm{d}\Omega - \oint_\Gamma \left[t_i \frac{\mathrm{d}u_i}{\mathrm{d}a} + u_i \frac{\mathrm{d}t_i}{\mathrm{d}a} \right] \mathrm{d}y \tag{11.13-a}$$

Part IV

FRACTURE MECHANICS OF CONCRETE

Chapter 12

FRACTURE DETERIORATION ANALYSIS OF CONCRETE

12.1 Introduction

1 It is ironic that although the foundation for fracture mechanics was laid by Griffith in the early thirties for brittle materials (such as concrete) (Griffith 1921), it has been mostly applied to metallic materials. Although there have been some pioneering efforts to apply fracture mechanics to concrete (Kaplan 1961), it was not until the mid-seventies that a number of researchers from the academic community focused their attention on various aspects of this application.

2 In applying fracture mechanics to concrete, much was initially borrowed from the wealth of information and research previously undertaken in conjunction with metals by metallurgists or mechanical engineers. However, it quickly became evident that by its very heterogeneous nature concrete has some unique fracture characteristics, which required the alteration of existing models.

3 By now fracture mechanics is universally acknowledged as a viable tool of analysis for investigation of concrete cracking. And after many years of development on numerous (plasticity based) constitutive models for concrete, tensile cracking remains its undisputed "Achille's heel". For the most part, even the simplest constitutive models appear to perform reasonably well under compressive regimes, however their capabilities are seriously challenged under tensile stresses. This apparent inability to properly model tensile cracking is of minor importance in reinforced concrete structures in which the steel "takes over" the tensile stresses.

4 However for unreinforced structures, such as dams, the apparent inability of the constitutive models to properly and efficiently model tensile cracking is a major handicap. As such for unreinforced concrete structures prone to tensile cracking, a fracture mechanics based model (rather than a plasticity based one) should be used.

5 Whereas an inappropriately large number of papers have been published on computational models for concrete (some of which will be discussed in a separate chapter), relatively few research has been undertaken to properly understand and characterize fracture models. Hence, this chapter will exclusively focus on the phenomenological aspects of concrete fracture from a material point of view.

(not necessarily corresponding to the loading direction). To accomplish this test a clip gage or a strain gage has to provide the feedback signal to the testing equipment in order to accordingly adjust the stroke.

10 Most concrete fracture tests are conducted under strain control with a gage located at the mouth of the crack providing the specimen response.

11 Both stroke and strain controlled tests require a closed-loop experimental set up, which is usually expensive and was not widely available until very recently.

12.2.2 Pre/Post-Peak Material Response of Steel and Concrete

12 As an introduction to concrete fracture, let us compare the pre- and post-peak response of metals and concrete, as illustrated in Fig.12.2, both obtained in a strain-controlled test of an uncracked or un-notched specimen.

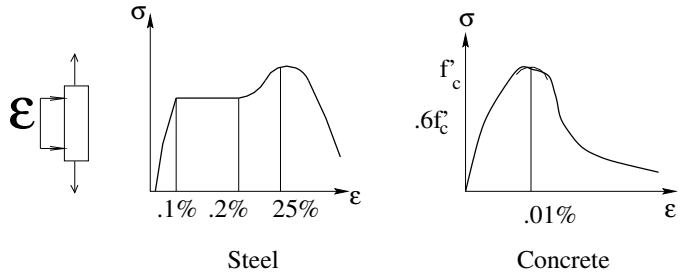

Figure 12.2: Stress-Strain Curves of Metals and Concrete

1. **Pre-peak**:
   (a) Metal exhibits a linear elastic response up to the yield stress σ_{yld}, and an approximate strain of 0.1%. Subsequently, due to internal dislocation plastic deformation with strain up to 25% may result to be followed by strain hardening.
   (b) Concrete exhibits a linear response up to approximately $0.6f'_t$. Subsequently, internal microcracking induces a nonlinear response up to a peak stress f'_t and a corresponding strain of approximately 0.01%.

   Under load control only the pre-peak response can be measured.

2. **Post-peak**:
   (a) Metals response in the post-peak zone is not yet well understood. Not only is it not of practical usefulness, but also it is largely overshadowed by necking.
   (b) Concrete response in the post-peak zone is most interesting, as it can exhibit additional strains. The descending branch of the concrete response in Fig. 12.2 is an idealization of the average material response. A more accurate description should account for the localization of the induced cracks. Thus away from the localized crack there is an elastic unloading, and at the crack, since a strain cannot be properly defined, a stress-crack opening displacement is a more appropriate model. This will be discussed in the subsequent section.

12.3.1.1 σ-COD Diagram, Hillerborg's Model

19 From the previous discussion, it is clear that concrete softening is characterized by a stress-crack opening width curve (and not stress-strain). The exact charachterization of the softening response should ideally be obtained from a uniaxial test of an uncracked specimen. However, it has been found (Li and Liang 1986, Hordijk, Reinhardt and Cornelissen 1989) that not only are those tests extremely sensitive, but drastically different results can be obtained from different geometries, sizes, and testing machines. Hence, the softening curve is often indirectly determined by testing notched specimens.

20 In what is probably the most referenced work in the nonlinear fracture of concrete literature, Hillerborg (Hillerborg, A. and Modéer, M. and Petersson, P.E. 1976) presented in 1976 a very simple and elegant model which has been previously described qualitatively. In this model, the crack is composed of two parts, Fig. 12.4:

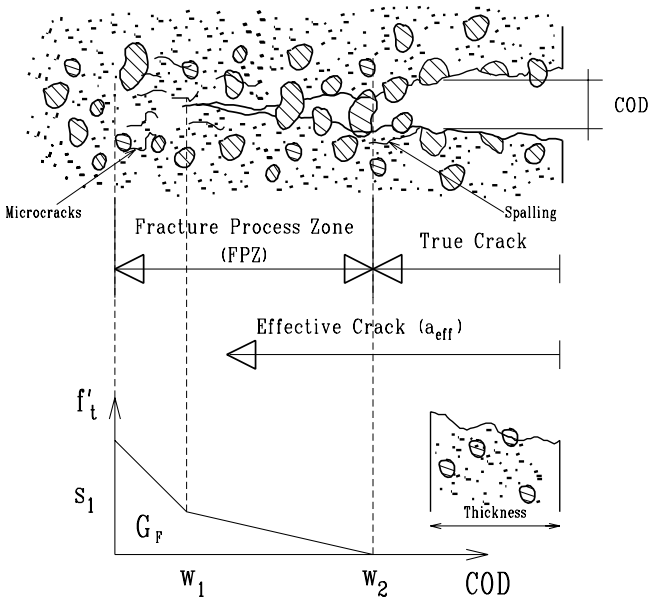

Figure 12.4: Hillerborg's Fictitious Crack Model

1. True or physical crack across which no stresses can be transmitted. Along this zone we have both displacement and stress discontinuities.
2. Fictitious crack, or Fracture Process Zone (FPZ) ahead of the previous one, characterized by:
   (a) peak stress at its tip equal to the tensile strength of concrete
   (b) decreasing stress distribution from f'_t at the tip of the fictitious crack to zero at the tip of the physical crack

   It should be noted that along the FPZ, we have displacement discontinuity and stress continuity.

13.1.2 Testing Procedure

10 Fracture toughness tests should be conducted under strain control where the strain is a measure of the crack mouth opening displacement[2] in a servo-controlled manner, Fig. 13.1.

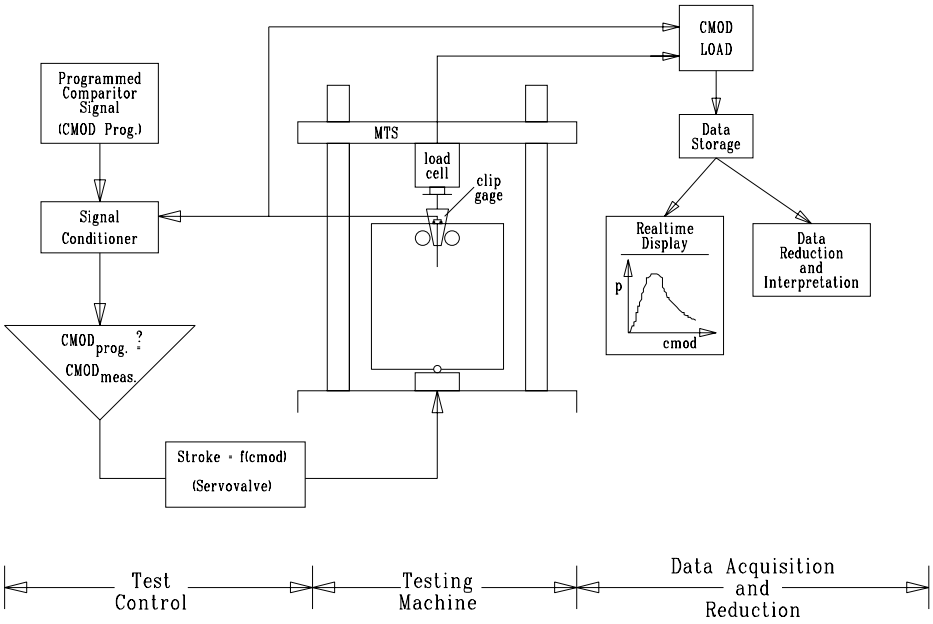

Figure 13.1: Servo-Controlled Test Setup for Concrete K_{Ic} and G_F

11 During the test, a plot of the load versus crack mouth opening displacement should be observed, Fig. 13.2.

12 The CMOD is first gradually increased. Following a linear part, a nonlinear prepeak response is first observed. This is associated with slow crack growth and thus the formation of a FPZ turning the notch into a crack. At around the peak load, the CMOD is decreased, thus effectively reducing the load. The load is then reapplied and the response would then extend into the post-peak regime. Throughout the descending branch of the structural softening, a series of unload and reload is performed in order to determine the experimental compliance of the cracked specimen for different crack lengths[3].

13.1.3 Data Reduction

Effective Young's modulus The effective crack length determination entails measurement of the specimen compliance (inverse of the stiffness or displacement over load). The compliance determination in turn requires the concrete Young's modulus.

The elastic modulus can be determined from:

[2] To conduct such tests under displacement control might result in undesirable snapbacks if the testing equipment is not rigid enough.

[3] Unload reload are not required for the experimental determination of G_F as this would simply be the area under the P-CMOD curve.

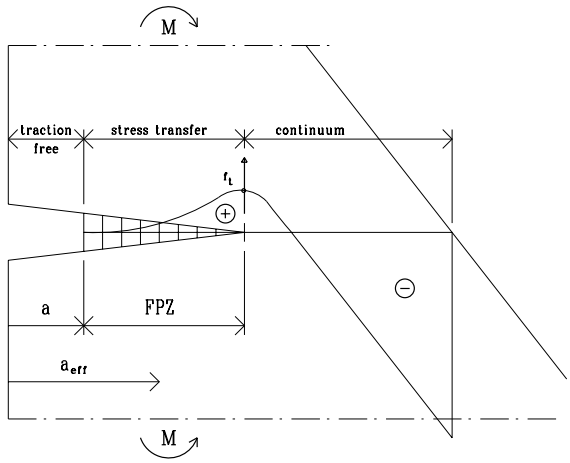

Figure 13.3: Effective Crack Length Definition

Compliance Derivative Method If the SIF were not derived from the finite element analysis, than the Compliance Derivative Method can be used to determine them. Recalling from Eq. 6.31 we have:

$$G = \frac{P^2}{2B}\frac{\partial C}{\partial a} \tag{13.6}$$

where P, a, C, and B are the applied load, crack length, compliance, and specimen width respectively. Combining Eq. 13.6 with $G = \frac{K_I^2}{E'}$ where $E' = E$ for plane stress and $E' = \frac{E}{1-\mu^2}$ for plane strain, we obtain:

$$K_I = \frac{E'P^2}{2B}\frac{\partial C}{\partial a} \tag{13.7}$$

Recalling that the experimental compliance is related to the normalized one through $C_n = EC_{exp}$, and assuming plane stress condition, Eq. 13.7 can be rearranged into:

$$K_I = \frac{P^2}{2B}\frac{\partial C_n}{\partial a} \tag{13.8}$$

This apparently simple and "elegant" method calls has a major drawback. Since the compliance is numerically approximated by Eq. 13.4, its derivative is very likely to be a very poor numerical approximation resulting in gross error when Eq. 13.8 is determined.

In summary, the initial unload reload will give E_{eff}, and each subsequent one will give a K_{Ic} corresponding to a different crack length. Thus more than one fracture toughness value can be obtained from a test whereas only one value of G_F can be obtained.

13.2 Nonlinear Fracture Models

13.2.1 Hillerborg Characteristic Length

13 The characteristic length, l_{ch}, proposed by Hillerborg (Hillerborg, A. and Modéer, M. and Petersson, P.E. 1976) in 1976 is a material property which gives an indication of the material

16 Thus in this simple, clear, and elegant model we implicitly account for softening by introducing a second parameter (CTOD), whereas in Hillerborg's approach the SIF concept is entirely discarded and replaced by a fictitious load, the distribution of which requires at least two parameters.

17 This model has been shown to yield results that are specimen size insensitive. A minor drawback of this model is that it requires an analytical expression of the COD and K_I along the crack for the geometry considered. In most cases this entails a finite element calibration.

18 This model requires an analytical expression for K_I and the $CTOD$ along the crack for each geometry considered, which in most cases can only be obtained through a finite element calibration. The model distinguishes between notch and crack length, and $CTOD_c$ is evaluated at the notch, thus the nonzero value for $CTOD_c$. Based on an extensive test program, the critical values, K_{Ic}^S and $CTOD_c$, were found to be size-independent material properties.

19 Finally, when combined with Young's Modulus, E, a single fracture parameter describing the material, termed the critical material length, Q, was derived:

$$Q = \left(\frac{E \cdot CTOD_c}{K_{Ic}^S} \right)^2 \tag{13.13}$$

The Q-value is related to the brittleness of the specimen. For large Q-values the material exhibits a high brittleness.

13.2.3 Size Effect Law, Bažant

Refer to chapter 14.

13.2.4 Carpinteri Brittleness Number

20 In fracture testing, failure may be caused by different mechanisms: (1) ultimate strength collapse (SOM), and, (2) fracture collapse in terms of LEFM. The dimensionless brittleness number, s, was developed by Carpinteri to assess the existence of either one of the two failure mechanisms (Carpinteri 1982a), (Carpinteri 1982b), (Carpinteri 1986). This parameter depends on the fracture toughness, K_{Ic}, the tensile strength, f_t', and on a dimension d characteristic of the specimen (or structure) geometry being considered:

$$s = \frac{K_{Ic}}{f_t' \sqrt{d}} \tag{13.14}$$

21 For large brittleness numbers, i.e., small specimen dimension d, SOM governs, and the interpretation of tests through Fracture Mechanics (FM) is not valid. Conversely, for small brittleness numbers, fracture mechanics is applicable since the specimen is more brittle. The boundary between SOM and FM applicability, is defined by the critical brittleness number, s_0, which is obtained from the nominal stress at failure.

13.3.2 Bažant Brittleness Number, β

27 The intersection between the SOM and LEFM approaches in the size effect diagram (Fig. 14.10) where

$$\sigma_N^{LEFM} = \sigma_N^{SOM} \tag{13.20}$$

defines the point where the brittleness number, β is equal to 1, or $d = \lambda_0 d_a = d_0$. From

$$K_{Ic} = D\frac{P^{max}}{t \cdot d}\sqrt{d} \tag{13.21}$$

$$\frac{P^{max}}{td} = \frac{K_{Ic}}{D\sqrt{d_0}} \tag{13.22}$$

and combining with

$$\frac{P^{max}}{t \cdot d} = \frac{\sigma_N}{C} \tag{13.23}$$

we obtain

$$\frac{P^{max}}{td} = \frac{Bf_t'}{C} \tag{13.24}$$

Eqs. 13.22 and 13.24 are combined into one equation, yielding:

$$\frac{f_t'^2 d_0}{K_{Ic}^2} = \left(\frac{C}{BD}\right)^2 = \mathcal{K}^2 \tag{13.25}$$

28 Because LEFM is assumed valid, substituting K_{Ic}^2 with $G_F \cdot E$ (Eq. 13.16), leads to:

$$\frac{f_t'^2 d_0}{G_F E} = \frac{d_0}{l_{ch}} = \mathcal{K}^2 \tag{13.26}$$

29 Thus, the brittleness number β used to assess the applicability of LEFM in the Size Effect Law can be related to Hillerborg's characteristic length, l_{ch}. Eq. 13.26 indicates that d/l_{ch} has a similar significance to the ratio between structural dimension d and maximum aggregate size d_a in the Size Effect Law. Since l_{ch} is a comprehensive parameter to describe material fracture, the d/d_a ratio in the Size Effect Law may be replaced by d/l_{ch} (Brühwiler, E., 1988). Comparison between the Size Effect Law and the Fictitious Crack Model showed that both models yield good agreement in the prediction of the size effect (Hillerborg, A. 1985b) and (Bažant 1985).

13.3.3 Carpinteri Brittleness Number, s

30 Squaring the expression s of the brittleness number (Eq. 13.14), and assuming that $K_{Ic}^2 = E \cdot G_F$, when LEFM is valid, the following expression is obtained:

$$s^2 = \frac{EG_F}{f_t'^2 d} = \frac{l_{ch}}{d} \tag{13.27}$$

or

$$s = \sqrt{\frac{l_{ch}}{d}} \tag{13.28}$$

1. Crack size: In a "large" crack, the effect of the process zone is smaller than for a "short" one. Thus LEFM is more applicable for the large ones.

2. Type of loading: If a structure is subjected to a load rather than imposed displacements (such as foundation settlements), than only a pre-peak response is of importance. Under those conditions non-linear effects may be negligible compared to the ones induced by LEFM.

3. Stability[5]: In a structure subjected to imposed load rather than imposed displacement non-linear effects are not be as negligible in a stable structure as they are in an unstable one.

Thus Table 13.2 provides some guidance for model selection. Accordingly we should select:

1. An NLFM for an arch dam which cracking is caused by foundation settlement.

2. An LEFM model for a dam in which cracking is caused by flooding, no matter how small or large the crack is.

Loading	"Small" Crack	"Large" Crack
Load Control, Unstable	LEFM	LEFM
Load Control, Stable	NLFM	LEFM
Displacement Control	NLFM	LEFM

Table 13.2: When to Use LEFM or NLFM Fracture Models

In all cases, it should be emphasized that ideally a non-linear analysis is to be undertaken, however in many (but not all) cases the complexity and expenses associated with such an analysis yield results very close to the ones obtained from a linear elastic ones. Thus ultimately the type of analysis to be undertaken hinges on both technical and economical considerations.

[5] A stable structure is one in which K_I decreases with crack length, in an unstable one the stress intensity factor K_I increases with crack length.

Chapter 14

SIZE EFFECT

`Paper in print`

1 Crack bridging occurs when cohesive stresses join the opposite faces of a crack, shielding the tip from the full effect of the applied load and thus giving rise to increased fracture resistance. Cohesive stresses are present both in elasto-plastic materials such as metals (through crack tip yielding), (Dugdale 1960), (Barenblatt 1962) and in quasi-brittle ones. In the later, they are present not only in cementitious materials, but also in ceramics, (Saouma, Natekar and Sbaizero 2002) and are caused by reinforcing fibers, particles (such as aggregates or inclusions), or simply regions of microscopically irregular crack surfaces causing topological interference.

2 Cohesive stress models were first suggested by Dugdale (1960) using a constant stress, then Barenblatt (1962) generalized this concept to a more general stress distribution, one which causes the crack faces to close smoothly. It should be noted that those two pioneering studies attributed different causes to the cohesive stresses. For Dugdale it was caused by macroscopic plasticity (and can be of any size) while for Barenblatt it was caused by molecular cohesion (and must be restricted to a relatively very small zone), (Kanninen and Popelar 1985). Finally, most recently Hillerborg, A. and Modéer, M. and Petersson, P.E. (1976) assumed a nonlinear model where the stress is a function of the crack opening. The first two models are most appropriate for metals to account for the presence of a plastic zone, whereas Hillerborg's model is more suited for cementitious material with a fracture process zone.

3 In both Dugdale and Barenblatt solution, the stress intensity factors caused by the far field load, and the cohesive stresses are assumed to cancel each other. Hence, implicit in this assumption is a zero material fracture toughness.

4 Finally, Hillerborg does not consider any singularity at the tip of the crack. Implicit in his approach is that there can not be a stress singularity at the crack tip since the criterion for crack propagation is based on the crack tip stress. This assumption was recently challenged by Xu and Reinhardt (1998) who developed the double-K criterion where $K_R(\Delta a) = K_{Ic}^{ini} + K^C(\Delta a)$ and $K^C(\Delta a) = F(f_t, f(\sigma), \Delta a)$. In this model, developed for concrete, the resistance to crack growth (right hand side) is first set to the inherent toughness, and then to a cohesive term. Hence, contrarily to Hillerborg's model, a cohesive stress does not necessarily eliminate the stress singularity, and as such crack propagation is no longer governed by a stress criteria, but rather by a modified linear elastic fracture mechanics one. This model enables us to distinguish between initial crack growth (in the absence of a fracture process zone) governed by K_{Ic}^{ini} and subsequent unstable crack growth in terms of $K_{Ic}^{ini} + K^C(\Delta a)$. Despite its appeal, this model

10 This derivation would be characterized as semi-analytical, since it combines an analytical derivation (albeit with some simplifying assumptions), and experimental derivation of constants too complicated to be derived analytically. Finally, this derivation does not explicitly reference a plasticity and/or a linear elastic fracture mechanics solution. Yet, those two solutions are ultimately asymptotic to the derived size effect law.

14.1 Analytical Derivation

11 In this section, an alternate derivation of the size effect law is presented. Whereas it hinges (for simplifying reasons) on Dugdale's or Barenblatt's model for the cohesive stresses (in lieu of Hillerborg's fracture energy), it will be shown that a purely analytical expression could be derived, hence problem specific numerical values of B can be obtained.

12 This approach is based on classical elasto-plastic fracture mechanics, (Broek 1986), where in its simplest form the stress intensity factors caused by the cohesive stresses (in a plastic zone or process zone), are assumed to cancel the ones caused by the far field load. Hence, contrarily to the original derivation by Bažant, the size effect law will be shown to have explicit roots in plasticity and linear elastic fracture mechanics theories. As a result, it will be shown that not only quasi-brittle materials exhibit a size effect, but elasto-plastic ones as well.

14.1.1 Constant Cohesive Stresses

14.1.1.1 Central Crack

13 Starting with a general case, we consider an infinite plate subjected to a far field uniform tensile stress σ and a crack of length $2a$, at the tip of which we have a uniform cohesive compressive stress (Dugdale type) equal to the tensile strength f'_t, Fig. 14.2.

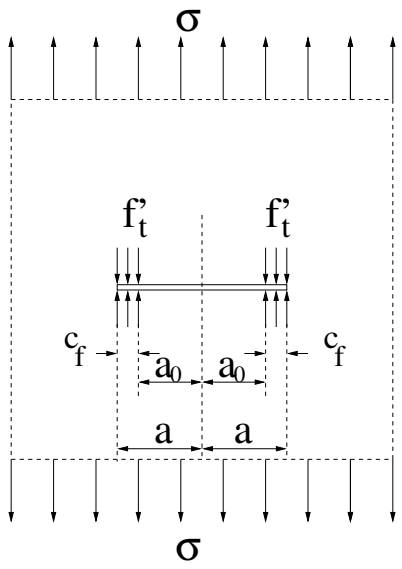

Figure 14.2: Central Crack With Constant Cohesive Stresses

14.1.1.2 Edge Crack

19 We next consider an arbitrary geometry of a cracked structure whose stress intensity factor due to the far field stress can be expressed as

$$K_a = \alpha\sigma\sqrt{\pi a} \tag{14.10}$$

where α is a coefficient which accounts for geometry, boundary conditions, and load.

20 On the other hand, the stress intensity factor corresponding to a constant stress, Fig. 14.4 is given by Stevens and Guiu (1994) as

$$K_b = -f_t'\sqrt{\pi a} f_b \tag{14.11}$$

where

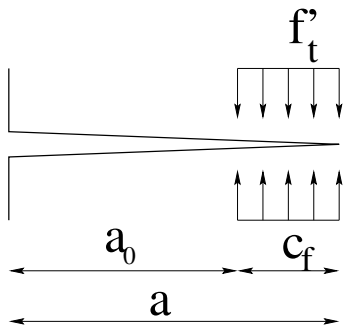

Figure 14.4: Dugdale's Model

$$\begin{aligned} f_b &= 0.903s^{1/2} + \frac{1}{3}0.4406s^{3/2} + \frac{1}{5}0.4997s^{5/2} - \frac{1}{7}0.1438s^{7/2} \\ &\quad -\frac{1}{9}0.04578s^{9/2} \end{aligned} \tag{14.12}$$

and $s = c_f/a$. Since at most $s = 1$, we keep only the first term which has an exponent lower than one.

21 Equating K_a to K_b, we solve for the far field nominal stress σ_n which would result in a zero net stress intensity factor at the tip of the crack. For this problem, we obtain

$$\sigma_n = \frac{0.903}{\alpha} f_t'\sqrt{s} \tag{14.13}$$

Expressed in terms of $r = a_0/c_f$, $s = 1/(1+r)$, the far field nominal stress will be

$$\sigma_n = \underbrace{\frac{0.903}{\alpha}}_{B} f_t' \sqrt{\frac{1}{1+\underbrace{r}_{\beta}}} \tag{14.14}$$

22 For an infinite plate with an edge crack, $\alpha = 1.1215$ (Tada et al. 1973), and the resulting nominal stress will be

$$\sigma_n = \underbrace{0.805}_{B} f_t' \sqrt{\frac{1}{1+\underbrace{r}_{\beta}}} \tag{14.15}$$

This equation is shown in Fig. 14.5.

$$K_b = \int_{a_0}^{a} K_b^P \mathrm{d}x = \frac{2}{\sqrt{\pi}} \int_{a_0}^{a} \frac{1 + F(x/a)}{\sqrt{a^2 - x^2}} \frac{x}{c_f} f_t' \sqrt{a} \mathrm{d}x \tag{14.18}$$

25 Equating this stress intensity factor caused by local plastification, to the far field stress intensity factor given by Eq. 14.10 (with $\alpha = 1.1215$) we solve for the nominal stress σ_n which would cause the net stress intensity factor to be equal to zero. Using $s = (a - a_0)/a$, and expanding in terms of s about $s = 0$, we obtain

$$\begin{aligned} \frac{\sigma_n}{f_t'} &= \frac{0.000124102}{s} - \frac{0.0000668046}{\sqrt{s}} - 0.000124102 + 0.535096\sqrt{s} \\ &\quad +0.0675175 s^{3/2} - 0.388195 s^{5/2} + 0.19108 s^{7/2} - 0.411846 s^{9/2} \\ &\quad +O[s]^5 \end{aligned} \tag{14.19}$$

26 Even though s is very small, we can drop the first three terms which are negligibly small compared to the others. This is first confirmed by replacing s with $1/(1 + r)$, and plotting Eq. 14.19
omitted, F
potential (

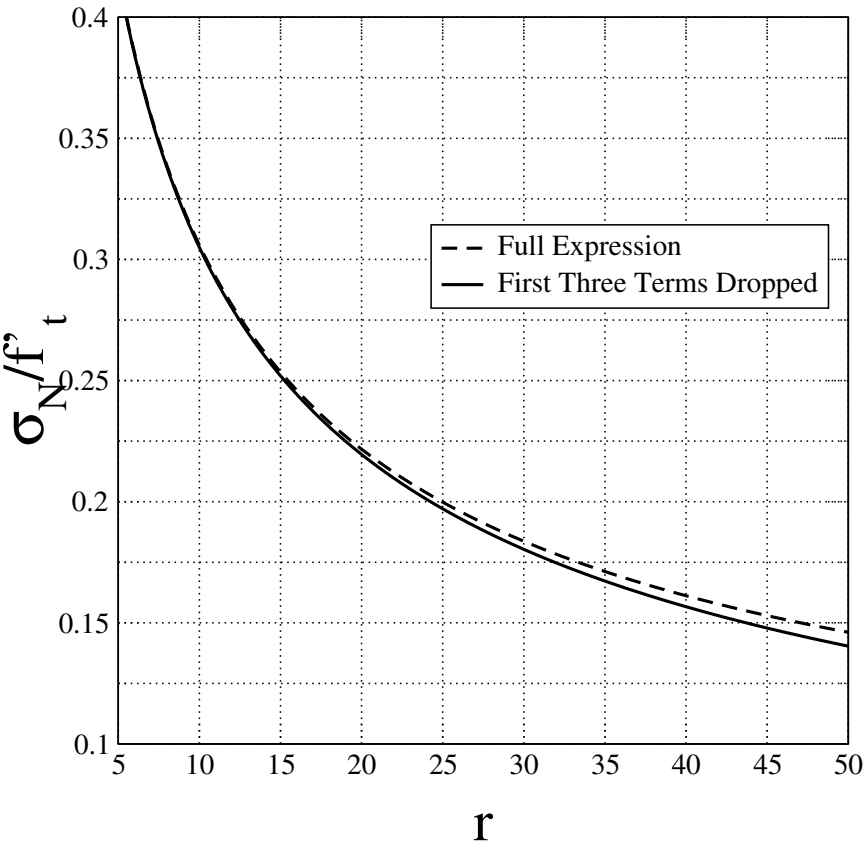

Figure 14.7: Energy Transfer During Infinitesimal Crack Extension

Hence, we may now justifiably drop the first three terms in Eq. 14.19, and rewrite this

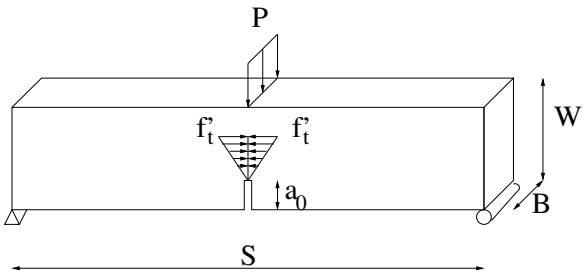

Figure 14.9: Three Point Bend Specimen with Linear Cohesive Stresses

30 The stress intensity factor for an edge crack subjected to a linearly varying cohesive stress (Barenblatt's type) K_b, Fig. 14.6 was given by Equation 14.18.

As before, equating the two stress intensity factors, solving for σ, substituting $s = (a - a_0)/a$, and expanding in terms of s about $s = 0$, we obtain

$$\begin{aligned} \frac{\sigma}{f'_t} &= -\frac{0.000067298}{s} + \frac{0.0000597828}{\sqrt{s}} + 0.000067298 + 1.06378\sqrt{s} \\ &\quad +8.32667 \times 10^{-17} s + 0.132783 s^{3/2} + O[s]^2 \end{aligned} \tag{14.25}$$

As for Eq. 14.19, it can be shown that we can retaining the terms in $s^{1/2}$ and $s^{3/2}$ without loss of accuracy, and thus obtain

$$\sigma_n = \frac{1.06738 f'_t}{\sqrt{1+r}} \left(1 + \frac{0.124401}{1+r} \right) + O[s]^2 \tag{14.26}$$

31 Again, this newly derived size effect law for a three point bend beam with a linearly varying cohesive stress along the fracture process zone is to be contrasted with Eq. 14.2. Should we drop the second term within the parenthesis, then and only then we will recover an equation analogous to Eq. 14.2.

14.2 Discussion

14.2.1 Comparison with Experimental Data

32 In order to assess the results, we closely examine experimental size effects tests on three point bending concrete specimens as reported in Table 1.5.2 of Bažant, Z. and Planas, J. (1998).

Table 14.1 gives the compressive strength and $B f'_t$. For the sake of simplification, we assume $f'_t = 0.1 f'_c$, and thus determine the experimental value of the B coefficient.

The average experimentally determined value is 1.39 (with a standard deviation of 0.61), and compares relatively well (given the assumption of a Barenblatt cohesive stress model) with the analytically derived value of 1.07 in Eq. 14.26. Interestingly enough, we note that the experimentally determined B value is clearly inversely proportional to the nominal specimen size D_0.

strength criterion governs.

3. Again for small structures (small β), $B = \frac{\sigma_N}{f'_t}$ and can be determined from plastic limit analysis.

4. For structures with very large size compared to aggregate size, $\frac{\lambda}{\lambda_0} \gg 1$. Thus Eq. 14.27 reduces to $f^*_t \simeq f'_t\sqrt{\frac{\lambda_0}{\lambda}}$, and we see that "For very large concrete structures, such as dams (or large rock masses), Eq. 14.27 asymptotically approaches the size effect of linear elastic fracture mechanics".

5. In general, Eq. 14.27 represents a gradual transition from the strength criterion for small structures to linear elastic fracture mechanics for large structures.

6. To assess the size effect law, geometrically identical specimens, but with different sizes must be tested. Then Eq. 14.27 can be cast in the form:

$$Y = a + b\lambda = \frac{1}{\sigma^2_N}, \tag{14.28}$$

where $a = \frac{1}{B^2}$ and $b = \frac{1}{B^2\lambda_0}$. From statistical regression analysis, the intercept a, and the slope b can be determined, and then $B = \frac{1}{\sqrt{a}}$ and $\lambda_0 = \frac{a}{b}$

7. If $\frac{\lambda}{\lambda_0} = \beta$ is less than 0.1, then a strength criterion must be used, and if β is greater than 10, then a LEFM criterion is to be used. Note that those are arbitrary guidelines.

8. The point of intersection of the two asymptotes corresponds to $\beta = 1$.

9. At no stage did we have to introduce (explicitly or implicitly) any LEFM equation (in the sense of a stress singularity at the crack tip).

10. The square root relationship between f^*_t and d (through λ) comes from:

    - an appropriate choice of the normalizing parameter for the crack length a in defining α_1 and α_2.
    - expression for G_F in terms of the square of f'_t in Eq. **??**. Although it is correct to directly relate G_F to the area under the uniaxial stress strain curve (a measure of the energy required to produce a unit surface), the square component is again not linked to LEFM.

11. It can be shown, (Bažant and Cedolin 1991) that the fracture energy G_F can be recovered from the Size Effect Law

12. There is a strong analogy between the size effect and column buckling, Fig. 14.11, Table 14.2.

14.2.3 LEFM vs NLFM Analyses

36 Ideally, we should extend the analytical solution to encompass Hillerborg's model as applied to a three point bending concrete specimen. To the best of the author's knowledge only two researchers addressed this complex nonlinear problem. Xu and Reinhardt (2000) developed a closed form solution, albeit an empirical one (as termed by its authors). Another solution was

presented by Karihaloo (1999) who again indirectly solved this problem, but with some rather restricting assumptions by enforcing a zero net stress intensity factor at the tip of the FPZ. Because of the restrictions imposed to those two solutions, the authors have not considered them in this study.

37 In a nonlinear fracture mechanics analysis the crack growth criteria is stress based, i.e the crack tip maximum tensile stress can not exceed the (non-zero) concrete tensile strength. Alternatively, in an LEFM analysis, we can set as a criteria a zero fracture toughness.

38 Whereas both criteria are readily accepted by the research community, practicing engineers have difficulties in accepting a non-zero tensile strength (hence rendering a NLFM analysis impossible), but can accept a small (preferably zero) fracture toughness, (Federal Regulatory Commission 1991) (in this context, the double-K method might be more acceptable to practicing engineers than solutions based on G_F and a non-zero f'_t). By the same token, a NLFM analysis should extend the fracture process zone to the point where the stress singularity no longer exists.

39 In order to highlight the duality between a zero fracture toughness criteria in an LEFM analysis, and a non-zero tensile strength criteria in a NLFM analysis a series of numerical analysis were performed. Considering a three point bend specimen, with G_F=100 N/m, f'_t=2 MPa, $S/W = 8$, $a/W = 0.6$, s_0=100 mm, beams with s_0, $10s_0$, $50s_0$ and $100s_0$ were analyzed using the code Merlin (Červenka, Reich and Saouma 1997–2003). Through those analyses, the two stress intensity factors K_a (caused by the external load) and K_b (caused by the cohesive Hillerborg's stress) were determined. Whereas contour integral techniques should be favored, one should be careful to leave a small zone at the tip of the crack traction free, otherwise the J integral will be equal to zero. Hence, in the context of this analysis (with surface traction on the crack faces) we used singular elements.

40 In each analysis, P_{max} corresponded to the onset of unstable crack growth (based on tensile stress at the crack tip), and the corresponding stress intensity factor K_{a+b} were determined. It should be noted that in our implementation of the interface element (based on the extended Hillerborg's model) pre-peak crack opening can occur. This results in a nonlinear pre-peak load-cod curve.

41 Whereas the variation of P_{max} with respect to s was indeed according to Bažant's size effect law, the net stress intensity factors at P_{max} ranged between 0.05 and 1.5 MPa$\sqrt{\text{mm}}$. Given that a representative value for the fracture toughness of concrete is about 1 MPa$\sqrt{\text{m}}$ or 31 MPa$\sqrt{\text{mm}}$, the net stress intensity factor can be considered as essentially zero. These values should be independent of the tensile strength, as a higher f'_t would result in a larger external load, and a higher K_a, but also in a higher (negative) K_b caused by the cohesive stresses. Indeed, when the tensile strength was increased from 2 MPa to 4 MPa, P_{max} was about twice the original values, however there was no discernable variation in K_{a+b}.

42 Thus, we conclude that for all practical purposes a NLFM analysis yields a very small non-zero stress intensity factor in comparison with fracture toughness. Hence, practicing engineers who accept a zero fracture toughness LEFM analysis should be reassured that a non-zero tensile strength in the context of a NLFM is, for all practical purposes, identical.

Chapter 15

FRACTALS, FRACTURES and SIZE EFFECTS

Adapted from (?)

15.1 Introduction

15.1.1 Fracture of Concrete

There is not yet a standard for concrete fracture testing although several have been proposed (RILEM, 1985). Concrete fracture properties include fracture toughness K_{Ic}, characteristic length l_{ch}, brittleness number β, fracture energy G_F, crack-tip opening displacement $CTOD$, and at least three additional parameters that characterize the concrete strain softening curve.

This chapter addresses a technique that uses fractal geometry to determine whether there is any surface indication of the direction of crack propagation in concrete and whether there is a correlation between fracture properties (K_{Ic} and G_F, which characterize the material resistance to cracking) and the roughness of the fracture surface as characterized by the fractal dimension D. The implications of the fractal nature of the cracked surface on the "true" fracture or surface energy are then discussed.

15.1.2 Fractal Geometry

Although most manmade objects have linear or smoothly curvilinear shapes, natural objects (such as rivers, mountains, clouds, and fractures) are commonly rough, fragmented, or discontinuous. The apparent randomness of these irregularities, coupled with our bias toward Euclidian geometry, handicapped us in studying and properly modeling such objects until the advent of fractal geometry (Mandelbrot, 1983) .

By definition, an inherent property of fractal objects is the statistical replication of patterns at different scales; a magnified part of a fractal object is statistically identical to the whole. Hence, Fig. 15.1-A illustrates the generation of a self-similar synthetic fractal curve, the triadic Koch curve.. First, an *initiator*, which represents an initial geometric form, is defined, then a *generator*, which describes a transformation on the initiator, is applied. As the transformation operation is repeatedly applied to the figure, a fractal curve is generated. For the triadic Koch curve, we note that at each step the number of line segments is increased by a factor of 4 and that the length of each new line segment generated is one third the length of line segments in the previous generation. This increases the total length of the fractal curve by four thirds

Table 16.2: Experimentally obtained material properties of the concrete mixes used.

MSA	f'_c, MPa (psi)	$f'_{t,sp}$, MPa(psi)	E_{eff}, MPa (ksi)
19-mm (0.75-in.)	25.6 (3,710)	2.81 (407)	18,000 (2,610)
38-mm (1.5-in.)	24.8 (3,600)	2.67 (388)	16,900 (2,460)
38-mm (1.5-in.) sub-angular	36.6 (5,317)	3.96 (574)	23,200 (3,360)
76-mm (3.0-in.)	18.9 (2,740)	2.41 (349)	16,500 (2,400)

Figure 16.1: *Wedge-splitting specimen geometry.

of small concrete specimens (Hillemeier & Hilsdorf 1976, Linsbauer & Tschegg 1986, Brühwiler 1988, Brühwiler & Wittmann 1990). The WS specimen has a large fracture area compared to the concrete volume, approximately 4.6 times greater than a commonly used three-point bend (TPB) beam geometry (RILEM 1985) of equal volume. The large fracture area compared to the aggregate size and specimen volume makes the WS geometry well suited for testing large MSA and specimens under laboratory conditions.

The dimensions of the WS specimens tested in the experimental program are summarized in Table 16.3. The specimen dimensions and aggregate sizes were selected to enable a comparison

Table 16.3: Wedge-splitting specimen dimensions.

Specimen Dimensions, cm (in.)							
Specimen Type	H	w	t	s	D	a_0	h
"Small"	31 (12.0)	31 (12.0)	23 (9.0)	6 (2.25)	3 (1.0)	4.5(1.75)	20 (8.0)
"Medium"	91 (36.0)	91 (36.0)	41 (16.0)	15 (6.0)	8 (3)	15.2 (6.0)	61 (24.0)
"Large"	152 (60.0)	152 (60.0)	41 (16.0)	15 (6.0)	8 (3)	30.5 (12.0)	107 (42.0)

with results previously obtained by other researchers in the academic community, and to predict fracture properties of dam concrete with intermediary values to ensure a continuity of results.

Specimen construction consisted of wooden formwork built for the placing of the concrete, a sharpened 3.2-mm (0.125-in.) thick steel plate mounted inside each form to obtain the vertical notch normal to the load line, and two hollow steel sleeves flanking the plate. Two different ready–mix suppliers delivered the concrete. The first provided the 19-mm and 38-mm MSA mixes and the other the 76-mm MSA concrete mix. In all specimens, with the exception of the cold-joint (CJ) specimens, the concrete was placed with the notch in the vertical direction, and cured at room temperature in the laboratory for at least 28 days prior to testing.

For the CJ specimens, the concrete was placed in two separate lifts, with the notch plate initially in a horizontal orientation. The tendency of the crack to propagate into the cold-joint, which is a region of inherent weakness, was studied through a slight offset between the initial notch and the level of the concrete in the first lift. Three days after the first lift was placed, the

16.2.3 Testing Procedure

The experimental setup of the electronic controller, the data acquisition system, and the testing machine for the WS specimen tests are shown in a simplified block diagram in Fig. 16.3. In the

Figure 16.3: *Block diagram of the experimental system.

WS specimen experiments, the primary deformation monitored was the crack–mouth opening displacement (CMOD). The CMOD was measured on the top surface of the specimen by a clip gage mounted over the mouth of the initial notch. The closed-loop servo-hydraulic test machine used a programmed constant rate of CMOD (1.0-μm/sec, or 40-μin/sec) as the feedback control to obtain stable crack growth with structural post-peak response. During the test, the vertical load and the CMOD were monitored and recorded using a standard data acquisition system. Unload/reload cycles, which were used to monitor the change in the specimen compliance, or flexibility, were performed. The experiment was performed until the specimen was split into two halves.

The vertical force induced by the wedge fixture, P_V, was directly obtained from the load cell of the testing machine. The wedge fixture is a statically determinate beam, and therefore, the splitting force is given by $P_{SP} = \frac{P_V}{2 \cdot \tan\alpha}$, where the wedge angle, α, is equal to 15°. (Frictional forces were neglected; they were reduced by using hardened steel inserts along the inclined wedge surface and needle bearings with a low coefficient of friction.) A typical P_{SP} vs. CMOD curve representative of the WS specimens is presented in Fig. 16.4. In the P_{SP} vs. CMOD

Figure 16.4: *Typical P_{SP} vs. CMOD curve for a “Large” specimen.

curve, both linear and nonlinear responses in the ascending prepeak branch and a descending postpeak branch can be observed.

16.2.4 Acoustic Emissions Monitoring

In several WS tests, the microcracking associated with fracture process zone (FPZ) formation and with transient releases of elastic energy due to localized aggregate fracture and bond failure were monitored with an acoustic emission (AE) sensor mounted on the surface of the specimen. Inside the sensor, a piezoelectric crystal is stimulated by the stress waves and produces electrical signals. The signals are then amplified, filtered, processed, and related to the behavior of the material throughout the experiment.

The AE sensor was mounted on the face of the specimen in a direction such that the sensor was normal to the predicted fracture plane. The sensor used during testing was sensitive in

Chapter 17

SINGULAR ELEMENT

17.1 Introduction

1 For most practical problems, either there is no analytical solution, or the handbook ((Tada et al. 1973)) ones are only crude approximation. Hence numerical techniques should be used. Whereas Boundary Element Methods are increasingly being used, (Aliabadi and Rooke 1991), they are far behind in sophistication the Finite Element Methods which will be exclusively covered in this chapter. For an overview of early finite element techniques in finite elements the reader should consult (Owen and Fawkes 1983), some of the more recent methods are partially covered in (Anderson 1995). Finally, the Ph.D. thesis of Reich (1993) and of **?** contain some of the major extensions of modern techniques to include thermal load, body forces, surface tractions in 2D and 3D respectively.

2 Numerical methods for fracture mechanics can be categorized in many different ways, in this chapter we shall use three criteria:

1. Those in which the singularity is modelled, that is the $r^{-\frac{1}{2}}$ stress field at the tip of the crack is properly represented.
2. Techniques in which the SIF are directly evaluated as part of the augmented global stiffness matrix.
3. Techniques through which the SIF can be computed *a post priori* following a standard finite element analysis via a special purpose post-processor.

17.2 Displacement Extrapolation

3 This technique was the predominant one prior to the serendipitous discovery of the quarter point singular element.

4 In early finite element studies of LEFM, it was recognized that unless singular elements could be used, it would necessitate to have a very fine mesh at the crack tip to approximate the stress singularity with non-singular elements.

5 Following a liner elastic analysis, the stress intensity factors were determined by equating the numerically obtained displacements with their analytical expression in terms of the SIF. Such

1. cover a brief review of the isoparametric element formulation
2. show how the element can be distorted in order to achieve a stress singularity
3. determine the order of the stress singularity
4. provide a brief review of all the historical developments surrounding this element
5. discuss the effect on numerical accuracy of element size, order of integration, and local meshing around the crack tip
6. briefly mention references to other singular elements

17.4 Review of Isoparametric Finite Elements

12 In the isoparametric finite element representation, both the internal displacement and coordinates are related to their nodal values through the shape functions:

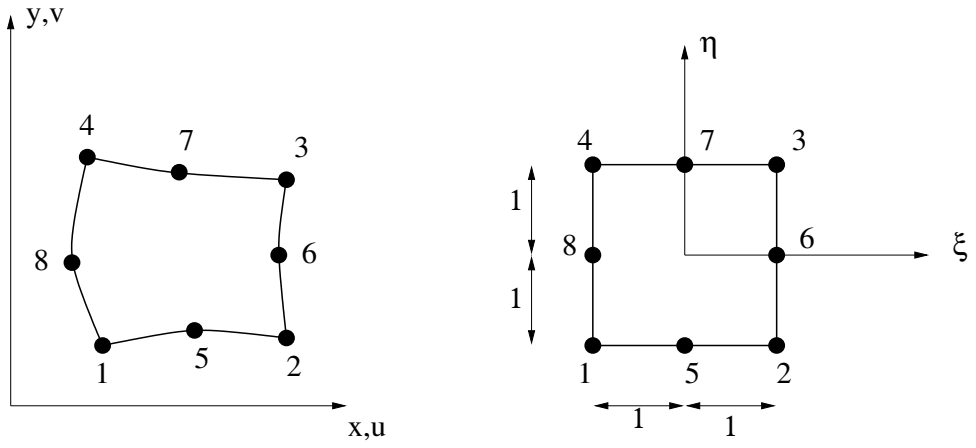

Figure 17.2: Isoparametric Quadratic Finite Element: Global and Parent Element

$$\left\{ \begin{array}{c} x \\ y \end{array} \right\} = \sum_{i=1}^{8} \left[\begin{array}{cc} N_i & 0 \\ 0 & N_i \end{array} \right] \left\{ \begin{array}{c} \overline{x}_i \\ \overline{y}_i \end{array} \right\} \tag{17.2}$$

$$\{d\} = \left\{ \begin{array}{c} u \\ v \end{array} \right\} = \sum_{i=1}^{8} \left[\begin{array}{cc} N_i & 0 \\ 0 & N_i \end{array} \right] \left\{ \begin{array}{c} \overline{u}_i \\ \overline{v}_i \end{array} \right\} \tag{17.3}$$

where the N_i are the assumed shape functions.

13 The shape functions are obtained by mere inspection (i.e. **serependitiously**),

$$\begin{array}{lcll} N_i & = & \frac{1}{4}\left(1+\xi\xi_i\right)\left(1+\eta\eta_i\right)\left(\xi\xi_i+\eta\eta_i-1\right) & i=1,2,3,4 \\ N_i & = & \frac{1}{2}\left(1-\xi^2\right)\left(1+\eta\eta_i\right) & i=5,7 \\ N_i & = & \frac{1}{2}\left(1+\xi\xi_i\right)\left(1+\eta^2\right) & i=6,8 \end{array} \tag{17.4}$$

and are tabulated in Table 17.1.

Chapter 18

ENERGY RELEASE BASED METHODS

1 In this class of solutions, we will exploit the definition of the energy release rate G to derive a simple method of determining the stress intensity factors. We shall distinguish between mode I and mixed mode cases. The former one, although of academic relevance only, is a simple introduction to the second.

18.1 Mode I Only

18.1.1 Energy Release Rate

2 Recalling that the strain energy release rate G is given by:

$$\boxed{G = -\frac{\partial U}{\partial a} = \frac{K_I^2}{E'} \simeq \frac{\Delta U}{\Delta a}} \tag{18.1}$$

a simple algorithm for the SIF calculation emerges:

1. For an initial crack length a, determine the total strain energy from either one of the following approaches:
   (a) $U = \mathbf{u}^t\mathbf{K}\mathbf{u}$ where $\mathbf{u}$ is nodal displacement, and $\mathbf{K}$ is the global structural stiffness matrix.
   (b) $U = \mathbf{u}^\mathbf{t}\mathbf{P}$ where $\mathbf{P}$ and $\mathbf{u}$ are the externally applied nodal load and displacement, respectively.
2. Increase the crack length from a to $a + \Delta a$, Fig. 18.1, and reanalyze.
3. Determine G from $G \simeq \frac{(U+\Delta U)-U}{(a+\Delta a)-a} = \frac{\Delta U}{\Delta a} = \frac{K_I^2}{E'}$

3 Note that:

1. This procedure requires two complete separate analyses.

Chapter 19

J INTEGRAL BASED METHODS

19.1 Numerical Evaluation

1 Within linear elastic fracture mechanics, the J integral is equivalent to G and we have:

$$G = J = -\frac{\partial \Pi}{\partial a} = \int_r (w \mathrm{d}y - \mathbf{t} \cdot \frac{\partial \mathbf{d}}{\partial x} \mathrm{d}s) \tag{19.1}$$

2 Thus it is evident that we do have two methods of evaluating J: the first one stems from its equivalence to the energy released rate, and the second one from its definition as an integral along a closed contour. Evaluation of J according to the first approach is identical to the one of G and has been previously presented.

3 In this chapter we shall present the algorithm to evaluate J on the basis of its contour line integral definition. Whereas derivation will be for J integral only, its extension to J_i is quite straightforward.

4 If the stresses were to be determined at the nodes, than the numerical evaluation of J will be relatively simple. However, most standard finite element codes only provide Gauss point stresses, and hence care must be exercised in properly determining the J integral along a path passing through them.

5 The algorithm for the J calculation closely follows the method presented in (Owen and Fawkes 1983), and is as follows:

1. First let us restrict ourselves to the more general case in which isoparametric elements are used. Because the stresses are most accurately evaluated at the gauss points, the path can be conveniently chosen to coincide with $\xi = \xi_{cst}$ and/or $\eta = \eta_{cst}$. For the sake of discussion, let us assume that the element connectivity is such that the path is along $\xi = \xi_{cst}$, as in Fig. 19.1. We note that for corner elements the integration will have to be performed twice along the two directions.

2. Now let us start from the basic definition of J:

$$J = \int_\Gamma w \mathrm{d}y - \mathbf{t} \cdot \frac{\partial \mathbf{d}}{\partial x} \mathrm{d}s \tag{19.2}$$

where $\mathbf{t}$ is the traction vector along $\mathbf{n}$, which is normal to the path; $\mathbf{d}$ is the displacement vector; $\mathrm{d}s$ is the element of arc along path Γ; and w is the strain energy density. We note

where n_1 and n_2 are the components of $\mathbf{n}$, which is a unit vector normal to the contour line at the Gauss point under consideration.

8. Having defined all the terms of J, we substitute in Eq. 19.2 to obtain the contribution to J from a particular Gauss point within an element.

$$\begin{aligned} J^e &= \int_{-1}^{1} \Bigg\{ \underbrace{\frac{1}{2}\left[\sigma_x \frac{\partial u}{\partial x} + \tau_{xy}\left(\frac{\partial u}{\partial y} + \frac{\partial v}{\partial x}\right) + \sigma_y \frac{\partial v}{\partial y}\right]}_{w} \underbrace{\frac{\partial y}{\partial \eta}}_{\mathrm{d}y} \\ &\quad - \underbrace{\left[(\sigma_x n_1 + \tau_{xy} n_2)\frac{\partial u}{\partial x} + (\tau_{xy} n_1 + \sigma_y n_2)\frac{\partial v}{\partial x}\right]}_{\mathbf{t}\cdot\frac{\partial \mathbf{d}}{\partial x}} \\ &\quad \underbrace{\sqrt{\left(\frac{\partial x}{\partial \eta}\right)^2 + \left(\frac{\partial y}{\partial \eta}\right)^2}}_{\mathrm{d}s} \Bigg\} \mathrm{d}\eta \\ &= \int_{-1}^{1} I \mathrm{d}\eta \end{aligned} \tag{19.9}$$

9. Since the integration is to be carried out numerically along the path (using the same integration points used for the element stiffness matrix), we have:

$$J^e = \sum_{q=1}^{NGAUS} I(\xi_p, \eta_q) W_q \tag{19.10}$$

where W_q is the weighting factor corresponding to η_q and $NGAUS$ is the order of integration (2 or 3).

10. Stresses $\sigma_x,\ \sigma_y,\ \tau_{xy}$ are readily available at the Gauss points.

11. $\frac{\partial u}{\partial x}$, $\frac{\partial u}{\partial y}$, $\frac{\partial v}{\partial x}$, and $\frac{\partial v}{\partial y}$ are obtained through the shape function. For instance $\frac{\partial u}{\partial x} = \lfloor \frac{\partial N_i}{\partial x} \rfloor \{u_i\}$ where the u_i are the nodal displacements and $\frac{\partial N_i}{\partial x}$ is the cartesian derivative of the shape function stored in the $[B]$ matrix:

$$[\mathbf{B}] = \begin{bmatrix} \frac{\partial N_i}{\partial x} & 0 \\ 0 & \frac{\partial N_i}{\partial y} \\ \frac{\partial N_i}{\partial y} & \frac{\partial N_i}{\partial x} \end{bmatrix} \tag{19.11}$$

where i ranges from 1 to 8 for quadrilateral elements.

12. Another term not yet defined in Eq. 19.9 is $\frac{\partial y}{\partial \eta}$. This term is actually stored already in the Gauss point Jacobian matrix:

$$[J] = \begin{bmatrix} \frac{\partial x}{\partial \xi} & \frac{\partial y}{\partial \xi} \\ \frac{\partial x}{\partial \eta} & \frac{\partial y}{\partial \eta} \end{bmatrix} \tag{19.12}$$

Chapter 20

RECIPROCAL WORK INTEGRALS

Chapter adapted from (Reich 1993)

20.1 General Formulation

1 In addition to conservation laws, a form of Betti's reciprocal work theorem (Sokolnikoff 1956) can also be exploited to directly compute stress intensity factors (Stern 1973). The reciprocal work theorem defines the relationship between two equilibrium states for a solid.

2 For a solid free of body forces and initial strains and stresses the reciprocal work theorem is defined as

$$\boxed{\oint_\Gamma t_i \, \tilde{u}_i \, \mathrm{d}\Gamma \;=\; \oint_\Gamma \tilde{t}_i \, u_i \, \mathrm{d}\Gamma} \tag{20.1}$$

where Ω is any simply connected region within the solid and Γ is the contour of that region; u_i and t_i are the displacements and surface tractions, respectively, associated with one equilibrium state and $\tilde{u}_i$; and $\tilde{t}_i$ are the displacements and surface tractions, respectively, associated with another equilibrium state.

3 The equilibrium state defined by u_i and t_i is called the primary state and the equilibrium state defined by $\tilde{u}_i$ and $\tilde{t}_i$ is called the complementary or auxiliary state.

4 To apply the reciprocal work theorem to a cracked solid the simply connected region Ω must be defined such that the singularity at the crack tip is avoided. This is accomplished by defining a pair of surfaces, Γ and Γ_ϵ, that begin on one crack surface and end on the other.

5 Γ is an arbitrary surface defined in the counter-clockwise direction around the crack tip but far away from it.

6 Γ_ϵ is a circle of radius ϵ centered on the crack tip that is defined in the clockwise direction around the crack tip completely inside Γ.

7 Another pair of surfaces, Γ_t^+ and Γ_t^-, corresponding to the crack surfaces complete the definition of Γ, as is shown in Figure 20.1. Γ_t^+ is defined on the upper crack surface between Γ and Γ_ϵ and Γ_t^- is defined on the lower crack surface bewteen Γ_ϵ and Γ.

Chapter 21

FICTITIOUS CRACK MODEL

Originally published as:
Implementation and Validation of a nonlinear fracture model in a 2D/3D finite element code by Reich, Plizzari, Cervenka and Saouma; in *Numerical Models in Fracture of Concrete*; Wittman Ed., Balkema (1993).

1 An incremental formulation for the Fictitious Crack Model (FCM) will be presented. The computational algorithm treats the structure as a set of sub-domains bonded along assumed crack paths. The crack paths are defined by interface elements that initially act as constraints enforcing the bond between adjacent sub-domains, but change state to function as standard interface elements as the crack propagates. Constraints are enforced on the global system of equations using a penalty approach.

2 A load scaling strategy, which allows for load controlled analyses in the post-peak regime, is used to enforce stress continuity at the tip of the Fracture Process Zone (FPZ).

3 To demonstrate the accuracy of the computational algorithm, a series of three wedge-splitting (WS) test specimens are analyzed. Specimen sizes are 31, 91, and 152 cm (1, 3, and 5 ft). Material properties for the concrete are taken as the mean values of the observed experimental results for all specimen sizes. The computed results are compared to the envelopes of the experimental response for each specimen size.

21.1 Introduction

4 The most commonly implemented nonlinear fracture model for concrete using the discrete crack approach is the FCM (Hillerborg, A. and Modéer, M. and Petersson, P.E. 1976). In the FCM the zone of micro-cracking and debonding ahead of the crack front is modeled as a cohesive stress that acts to close the crack. The magnitude of the cohesive stresses on the crack surface are determined by a softening law that relates the stress to the relative displacement of the crack surfaces through the fracture energy.

5 Many implementations of the FCM have been reported (Ingraffea and Gerstle 1984, Roelfstra and Sadouki 1986, Dahlblom and Ottosen 1990, Bocca, Carpinteri and Valente 1990, Gopalaratnam and Ye 1991, Gerstle and Xie 1992), but none of the implementations based on a discrete

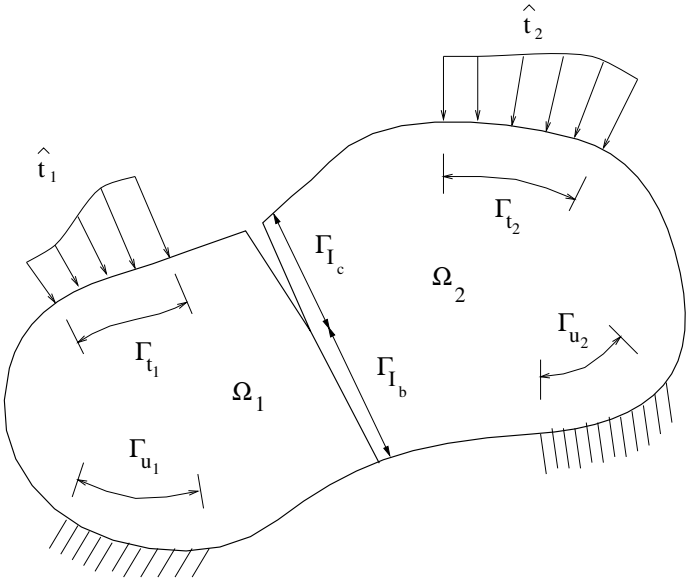

Figure 21.1: Body Consisting of Two Sub-domains

10 Defining the interface surface as

$$\Gamma_I = \Gamma_{I_b} \cup \Gamma_{I_c}, \tag{21.6}$$

where Γ_{I_b} is the bonded interface surface and Γ_{I_c} is the interface surface subject to cohesive stresses, the external work on the interface is written as

$$\int_{\Gamma_I} \delta \mathbf{u}_1^T \mathbf{t}_{I_1} d\Gamma = \int_{\Gamma_{I_b}} \delta \mathbf{u}_1^T \mathbf{t}_b d\Gamma + \int_{\Gamma_{I_c}} \delta \mathbf{u}_1^T \mathbf{t}_c d\Gamma \tag{21.7-a}$$

$$\int_{\Gamma_I} \delta \mathbf{u}_2^T \mathbf{t}_{I_2} d\Gamma = -\int_{\Gamma_{I_b}} \delta \mathbf{u}_2^T \mathbf{t}_b d\Gamma - \int_{\Gamma_{I_c}} \delta \mathbf{u}_2^T \mathbf{t}_c d\Gamma \tag{21.7-b}$$

Both $\mathbf{t}_b$ and $\mathbf{t}_c$ are unknown, but as $\mathbf{t}_b$ acts on the bonded, or constrained, interface it will be treated as a Lagrange multiplier

$$\boldsymbol{\lambda} = \mathbf{t}_b \tag{21.8}$$

11 Substituting $\boldsymbol{\lambda}$ into Equations 21.3 and 21.4-a-21.4-c and including the external work performed by the surface tractions on the interface surface, the Principle of Virtual Work for sub-domains Ω_1 and Ω_2 is written as

$$\boxed{\begin{aligned} \int_{\Omega_1} \delta \boldsymbol{\epsilon}_1^T \boldsymbol{\sigma}_1 d\Omega - \int_{\Omega_1} \delta \mathbf{u}_1^T \mathbf{b}_1 d\Omega - \int_{\Gamma_{t_1}} \delta \mathbf{u}_1^T \hat{\mathbf{t}}_1 d\Gamma - \int_{\Gamma_{I_b}} \delta \mathbf{u}_1^T \boldsymbol{\lambda} d\Gamma - \int_{\Gamma_{I_c}} \delta \mathbf{u}_1^T \mathbf{t}_c d\Gamma &= 0 \\ \int_{\Omega_2} \delta \boldsymbol{\epsilon}_2^T \boldsymbol{\sigma}_2 d\Omega - \int_{\Omega_2} \delta \mathbf{u}_2^T \mathbf{b}_2 d\Omega - \int_{\Gamma_{t_2}} \delta \mathbf{u}_2^T \hat{\mathbf{t}}_2 d\Gamma + \int_{\Gamma_{I_b}} \delta \mathbf{u}_2^T \boldsymbol{\lambda} d\Gamma + \int_{\Gamma_{I_c}} \delta \mathbf{u}_2^T \mathbf{t}_c d\Gamma &= 0 \end{aligned}} \tag{21.9}$$

12 On Γ_{I_b} the displacements for the two sub-domains, $\mathbf{u}_1 |_{\Gamma_{I_b}}$ and $\mathbf{u}_2 |_{\Gamma_{I_b}}$, must be equal. This condition can be written as a constraint in the strong form

$$\mathbf{u}_2 |_{\Gamma_{I_b}} - \mathbf{u}_1 |_{\Gamma_{I_b}} = \mathbf{0}, \tag{21.10}$$

Chapter 22

INTERFACE CRACK MODEL

`This chapter was chapter 6 of the PhD thesis of Cervenka`

1 This chapter discusses the nonlinear modeling of concrete using a discrete crack fracture mechanics based model. It addresses two important issues: mixed mode fracture in homogeneous materials and interface fracture. A new three-dimensional interface crack model is derived. The model is a generalization of classical Hillerborg's fictitious crack model, which can be recovered if shear displacements are set to zero. Several examples are used to validate the applicability of the proposed interface crack model. First, direct shear tests on mortar joints are used to test the model performance in the shear-compression regime. The more complicated combination of shear-tension is investigated using large biaxial tests of concrete-rock interfaces. The applicability to mixed mode cracking in homogeneous concrete is tested using experiments on modified Iosipescu's shear beam and anchor bolt pull-out tests.

22.1 Introduction

2 The assumption of singular stresses at the crack tip is mathematically correct only within the framework of linear elastic fracture mechanics, but physically unrealistic.

3 In concrete materials, a fracture process zone (Section **??**) exists ahead of the crack tip. The most popular model simulating this behavior is Hillerborg's fictitious crack model (FCM) described in Section **??** and Figure **??**. In a previous work, the classical FCM model was implemented by (Reich 1993) for mode I crack propagation, and extended to account for the influence of water pressure inside the crack.

4 The classical FCM model, Chapter 21, defines a relationship between normal crack opening and normal cohesive stresses, and assumes that there are no sliding displacements nor shear stresses along the process zone. This assumption is only partially valid for concrete materials. Based on experimental observations, it is indeed correct that a crack is usually initiated in pure mode I (i.e. opening mode) in concrete, even for mixed mode loading. However, during crack propagation, the crack may curve due to stress redistribution or non-proportional loading, and significant sliding displacements develop along the crack as schematically shown in Figure 22.1. Therefore, it is desirable to incorporate these shear effects into the proposed crack model.

5 Finally for concrete dams, it is well accepted that the weakest part of the structure is the dam-foundation interface, which is also the location of highest tensile stresses and lowest tensile

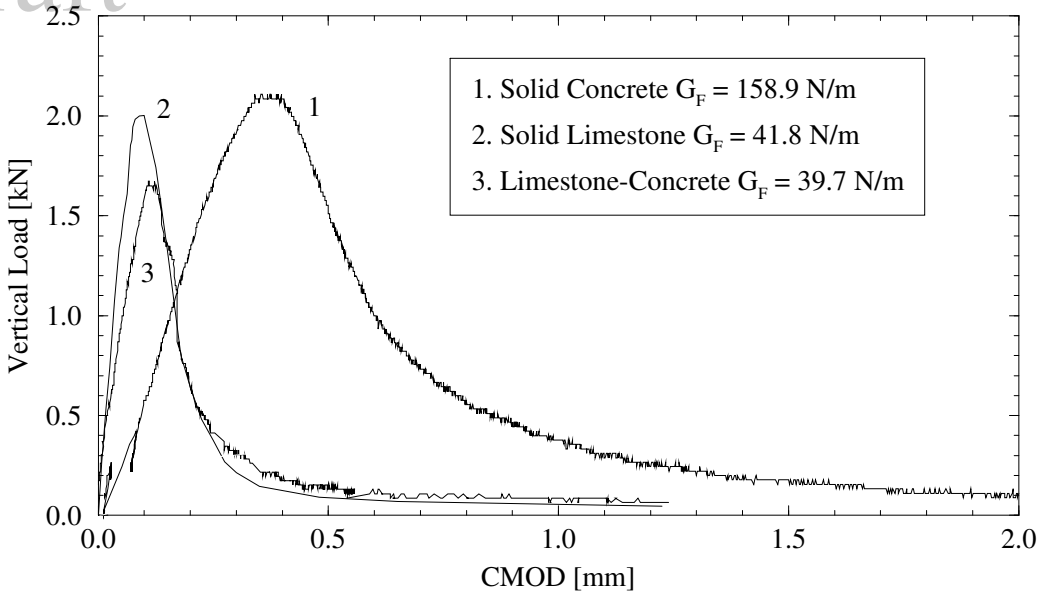

Figure 22.2: Wedge splitting tests for different materials, (Saouma V.E., and Červenka, J. and Slowik, V. and Chandra Kishen, J.M. 1994)

is not abrupt, but is rather gradual. This is caused by the presence of the fracture process zone, along which the energy of the system is gradually dissipated.

12 In the present model, the rock-concrete contact is idealized as an interface between two dissimilar materials with zero thickness. Thus, the objective is to define relationships between normal and tangential stresses with opening and sliding displacements. The notation used in the interface model is illustrated in Figure 22.2.

13 The major premises upon which the model is developed are:

(1) Shear strength depends on the normal stress.

(2) Softening is present both in shear and tension.

(3) There is a residual shear strength due to the friction along the interface, which depends on the compressive normal stress.

(4) Reduction in strength, i.e. softening, is caused by crack formation.

(5) There is a zero normal and shear stiffness when the interface is totally destroyed.

(6) Under compressive normal stresses neither the shear and nor the normal stiffnesses decrease to zero. In addition, should a compressive stress be introduced in the normal direction following a full crack opening, two faces of the interface come to contact, and both tangential and normal stiffnesses become nonzero.

(7) Irreversible relative displacements are caused by broken segments of the interface material and by friction between the two crack surfaces.

(8) Roughness of the interface causes opening displacements (i.e. dilatancy) when subjected to sliding displacements.

(9) The dilatancy vanishes with increasing sliding or opening displacements.

14 Figure 22.4 illustrates the probable character of the fracturing process along an interface.

15 In the proposed model the strength of an interface is described by a failure function:

$$F = (\tau_1^2 + \tau_2^2) - 2\,c\,\tan(\phi_f)(\sigma_t - \sigma) - \tan^2(\phi_f)(\sigma^2 - \sigma_t^2) = 0 \tag{22.1}$$

where:

- c is the cohesion.
- ϕ_f is the angle of friction.
- σ_t is the tensile strength of the interface.
- τ_1 and τ_2 are the two tangential components of the interface traction vector.
- σ is the normal traction component.

16 The shape of the failure function in two-dimensional case is shown in Figure 22.5, and it corresponds to the failure criteria first proposed by (Carol, I., Bažant, Z.P. and Prat, P.C., 1992). The general three-dimensional failure function is obtained by mere rotation around the σ-axis.

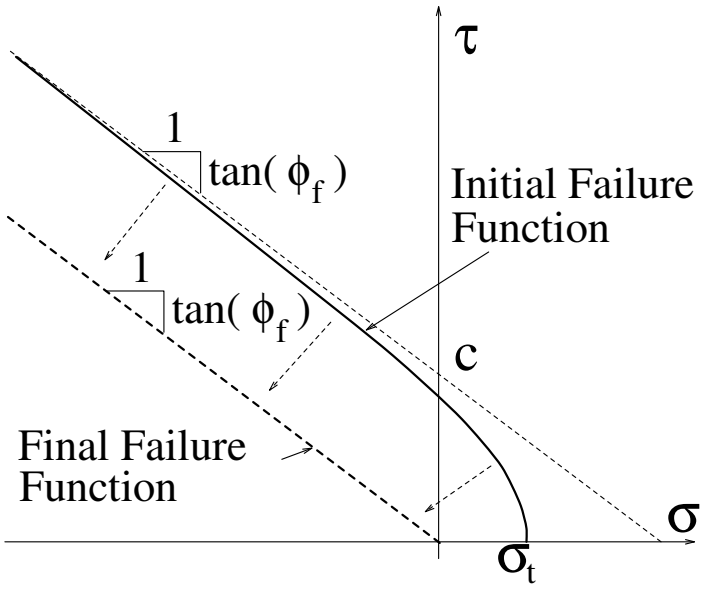

Figure 22.5: Failure function.

17 The evolution of the failure function is based on a softening parameter u^{ieff} which is the norm of the inelastic displacement vector $\boldsymbol{u}^i$. The inelastic displacement vector is obtained by decomposition of the displacement vector $\boldsymbol{u}$ into an elastic part $\boldsymbol{u}^e$ and an inelastic part $\boldsymbol{u}^i$. The inelastic part can subsequently be decomposed into plastic (i.e. irreversible) displacements $\boldsymbol{u}^p$ and fracturing displacements $\boldsymbol{u}^f$. The plastic displacements are assumed to be caused by friction between crack surfaces and the fracturing displacements by the formation of microcracks.

$$\begin{gathered} F = F(c, \sigma_t, \phi_f), \quad c = c(u^{\text{ieff}}), \quad \sigma_t = \sigma_t(u^{\text{ieff}}) \\ \boldsymbol{u} = \boldsymbol{u}^e + \boldsymbol{u}^i, \quad \boldsymbol{u}^i = \boldsymbol{u}^p + \boldsymbol{u}^f \\ u^{\text{ieff}} = ||\boldsymbol{u}^i|| = ({u_x^i}^2 + {u_y^i}^2 + {u_z^i}^2)^{1/2} \end{gathered} \tag{22.2}$$

Bibliography

399, A.: n.d., *Standard Test Method for Plane Strain Fracture Toughness of Metallic Materials, E399–74*, Annual Book of ASTM Standards.

446, A. C.: 1991, Fracture mechanics of concrete: Concepts, models and deformation of material properties, *Technical Report ACI 446.1R-91*, American Concrete Institute, Detroit, MI.

Abramowitz, M. and Stegun, I.: 1970, Handbook of mathematical functions, *Technical report*, National Bureau of Standard. Applied Mathematics Series, No. 55.

Advani, S. and Lee, K.: 1979, Thermo-mechanical failure criteria for rock media, pp. 19–25.

Aliabadi, M. and Rooke, D.: 1991, *Numerical Fracture Mechanics*, Kluwer Academic Publishers.

Alvaredo, A. and Wittman, F.: 1992, Crack formation due to hygral gradients, *Third International Workshop on Behaviour of Concrete Elements Under Thermal and Hygral Gradients*, Weimar, Germany.

Anderson, T.: 1995, *Fracture Mechanics, Fundamentals and Applications*, CRC Press.

Anon.: 1985, RILEM Draft Recommendation (50–FCM): Determination of the Fracture Energy of Mortar and Concrete by Means of Three–Point Bend Tests on Notched Beams, *Materials and Structures* **18**, 287–290.

Apostal, M.: 1974, *Development of an Anisotropic Singularity Finite Element Utilizing the Hybrid Displacement Method*, PhD thesis, State University of New York.

Atkinson, C. and Bastero, J.: 1991, On the use of betti's reciprocal theorem for computing the coefficients of stress singularities in anisotropic media, *International Journal of Engineering Science* **29**(6), 727–741.

Atkinson, C., Bastero, J. and Martinez-Esnaola, J.: 1988, Stress analysis in sharp angular notches using auxiliary fields, *Engineering Fracture Mechanics* **31**(4), 637–646.

Atkinson, C., Bastero, J. and Miranda, I.: 1986, Path-independent integrals in fracture dynamics using auxiliary fields, *Engineering Fracture Mechanics* **25**(1), 53–62.

Atkinson, C. and Craster, R.: 1992, The application of invariant integrals in diffusive elastic solids, *Philosophical Transactions of the Royal Society of London, Series A* **399**(1653), 231–263.

Atluri, S.: 1982, Path-independent integrals in finite elasticity and inelasticity, with body forces, inertia, and arbitrary crack-face conditions, *Engineering Fracture Mechanics* **16**(3), 341–364.

Bažant, Z.: 1985, Comment on hillerborg's comparison of size effect law with fictitious crack model, *in 'Dei Poli Anniversary Volume' edited by L. Cedolin, Politecnico di Milano* pp. 335–338.

Bažant, Z. and Cedolin, L.: 1991, *Stability of Structures*, Oxford University Press.

Bažant, Z. (ed.): 1992, *Proceedings of the First International Conference on Fracture Mechanics for Concrete and Concrete Structures*, Elsevier, Breckenridge, CO.

Bažant, Z. and Pfeiffer, P.: 1987, Determination of fracture energy properties from size effect and brittleness number, *ACI Material Journal* **84**(6), 463–480.

Bažant, Z. and Planas, J.: 1998, *Fracture and Size Effect in Concrete and Other Quasibrittle Materials*, CRC Press.

Bažant, Z.P.: 1984, Size effect in blunt fracture: Concrete, rock, metal, *J. of Engineering Mechanics, ASCE* **110**(4), 518–535.

Bažant, Z.P. and Cedolin, L.: 1979, Blunt crack propagation in finite element analysis, *J. of the Engineering Mechanics Division, ASCE* **105**, 297–315.

Benzley, S.: 1974, Representation of singularities with isoparametric finite elements, *Int. J. Num. Meth. Engng.* **8**, 537.

Bocca, P., Carpinteri, A. and Valente, S.: 1990, Size effects in the mixed mode crack propagation: Softening and snap-back analysis, *Engineering Fracture Mechanics* **35**(1–3), 159–170.

Bouchaud, E., Lapasset, G. and Planès, J.: 1990, Fractal dimension of fractured surfaces: a universal value?, *Europhysics Letters* **13**(1), 73–79.

Bourdarot, E., Mazars, J. and Saouma, V. (eds): 1994, *Proceedings of the International Workshop on Dam Fracture and Damage*, Balkema.

British Standards Institution, BS 5447, London: 1977.

Broek, D.: 1986, *Elementary Engineering Fracture Mechanics, 4th Edition*, Martinus Nijhoff Publishers.

Broek, D.: 1989, *The Practical Use of Fracture Mechanics*, Kluwer Academic Publishers.

Brown, S.: 1987, A note on the description of surface roughness using fractal dimension, *Geophysical Research Letters* **14**(11), 1095–1098.

Brown, S.: 1988, Correction to: A note on the description of surface roughness using fractal dimension, *Geophysical Research Letters* **15**(11), 286.

Brühwiler, E.,: 1988, *Fracture Mechanics of Dam Concrete Subjected to Quasi-Static and Seismic Loading Conditions*, Doctoral Thesis No 739, Swiss Federal Institute of Technology, Lausanne. (in German).

Brühwiler, E., Broz, J.J., and Saouma, V.E.,: 1991, Fracture model evaluation of dam concrete, *ASCE, Journal of Civil Engineering Materials* **4**, 235–251.

deLorenzi, H.G.: 1985, Energy release rate calculations by the finite element method, *Engineering Fracture Mechanics* **21**, 103–110.

Duda, H.: 1990, Stress-crack-opening relation and size effect in high-strength concrete, *Darmastad Concrete* **5**, 35–46.

Duga, J., Fisher, W., Buxbam, R., Rosenfield, A., Buhr, A., Honton, E. and McMillan, S.: 1983, The economic effects of fracture in the united states, *Technical Report SP647-2*, National Bureau of Standards.

Dugdale, D.: 1960, Yielding of steel sheets containing slits, *J. Mech. Phys. Sol.* **8**, 100–108.

Dunders, J.: 1969, Edge - bonded dissimilar orthogonal elastic wedges under normal and shear loading, *Journal of Applied Mechanics* **36**, 650–652.

Erdogan, F. and Sih, G.C.: 1963, On the crack extension in plates under plane loading and transverse shear, *Journal of Basic Engineering* **85**, 519–527.

Eshelby, J.: 1974, Calculation of energy release rate, *Prospect of Fracture Mechanics Nordhoff* pp. 69–84.

Fawkes, A., Owen, D. and Luxmoore, A.: 1979, An assessment of crack tip singularity models for use with isoparametric elements, *Eng. Fract. Mech.* **11**, 143–159.

Feder, J.: 1988, *Fractals*, Plenum Press.

Federal Regulatory Commission: 1991, Engineering guidelines for the evaluation of hydropower projects, *Technical report*, Federal Energy Regulatory Commission, Office of Hydropower Licensing.

Feenstra P.H., d. B. R. and J., R.: 1991, Numerical study on crack dilatancy. i: Models and stability analysis. ii: Applications, *J. Eng. Mech.* **117**(4), 733–769.

Foreman, R., Kearney, V. and Engle, R.: 1967, Numerical analysis of crack propagation in cyclic-loaded structures, *J. of Basic Engineering* **89**, 459–464.

Freese, C. and Tracy, D.: 1976, The natural isoparametric triangle versus collapsed quadrilateral for elastic crack analysis, *Int. J. Fract.* **12**, 768–770.

Gallagher, R.: 1975, *Finite Element Analysis Fundamentals*, Prentice Hall, Englewood Cliffs, N.J.

Gdoutos, E.: 1993, *Fracture Mechanics; An Introduction*, Kluwer Academic Press.

Gerstle, W. and Xie, M.: 1992, Fem modeling of fictitious propagation in concrete, *Journal of Engineering Mechanics* **118**(2), 416–434.

Giuriani, E. and Rosati, G. P.: 1986, Behaviour of concrete elements under tension after cracking, *Studi e Ricerche, Corso di Perfezionamento per le Costruzioni in Cemento Armato* **8**, 65–82. (in Italian).

Goodman, R.E., Taylor, R.C. and Brekke, T.C.,: 1968, A Model for the Mechanics of Jointed Rocks, *J. Soil Mech. Div., ASCE* **94**.

Hudson, C. and Seward, S.: 1978, *A Compendium of Sources of Fracture Toughness and Fatigue Crack Growth Data for Metallic alloys*, Vol. 14, Int. J. of Fracture.

Hudson, C. and Seward, S.: 1982, A compendium of sources of fracture toughness and fatigue crack growth data for metallic alloys, *Int. J. of Fracture, Part II* **20**, R59–R117.

Hussain, M., Pu, S. and Underwood, J.: 1974, Strain energy release rate for a crack under combined mode i and mode ii, *ASTM, STP 560* pp. 2–28.

Hussain, M., Vasilakis, J. and Pu, L.: 1981, Quadratic and cubic transition elements, *Int. J. Num. Meth. Engng.* **16**, 1397–1406.

Hutchinson, J.: 1968, Singular behavior at the end of a tensile crack tip in a power-law hardening material, *Journal of Mechanics and Physics of Solids* **16**, 13–31.

Hutchinson, J. W. and Suo, Z.: 1992, Mixed mode cracking in layered materials, *Advances in Applied Mechanics* **29**, 63–191.

Il'yushin, A.: 1946, The theory of small elastic-plastic deformations, *Prikadnaia Matematika i Mekhanika, PMM* **10**, 347–356.

Inglis, C.: 1913, Stresses in a plate due to the presence of cracks and sharp corners, *Trans. Inst. Naval Architects* **55**, 219–241.

Ingraffea, A.: 1977, *Discrete Fracture Propagation in Rocks: Laboratory Tests and Finite Element Analysis*, PhD thesis, University of Colorado.

Ingraffea, A. and Gerstle, W.: 1984, Non-linear fracture models for discrete crack propagation, *in* S. Shah (ed.), *Proceedings of the NATO Advanced Workshop on Application of Fracture Mechanics to Cementitious Composites*, Martinus Nijhoff, Hingham, Mass, pp. 171–209.

Ingraffea, A. and Manu, C.: 1980, Stress intensity factor computation in three dimension with quarter-point elements, *Int. J. num. Meth. Engng.* **15**(10), 1427–1445.

International Conference on Fracture and Damage of Concrete and Rock: 1988, Vienna. To be Published in Engineering Fracture Mechanics.

Irwin, G.: 1957, Analysis of stresses and strains near the end of a crack traversing a plate, *Transactions ASME, J. Appl. Mech.* **24**.

Irwin, G.: 1960, Plastic zone near a crack and fracture toughness, *Proc. 7th Sagamore Conf.*, p. 63.

Irwin, G.: 1962, The crack extension force for a part through crack in a plate, *Transactions ASME, J. Appl. Mech.* **29**.

Ishikawa, H.: 1980, A finite element analysis of stress intensity factors for combined tensile and shear loading by only a virtual crack extension, *Int. J. Fracture* **16**.

Issa, M., Hammad, A. and Chudnovsky, A.: 1993, Correlation between crack tortuosity and fracture toughness in cementitious materials, *International Journal of Fracture* **60**, 97–105.

Jeang, F. L. and Hawkins, N. M.: 1985, Nonlinear analysis of concrete fracture, *Structures and mechanics report*, Department of Civil Engineering, University of Washington, Seattle, WA.

Lotfi, H.: 1992, *Finite Element Analysis of Fracture of Concrete and Masonry Structures*, PhD thesis, University of Colorado, Boulder.

Lynn, P. and Ingraffea, A.: 1977, Transition elements to be used with quarter-point crack-tip elements, *Int. J. num. Meth. Engng.* **11**, 1031–1036.

Malyshew, B. M. and Salganik, R. L.: 1965, The strength of adhesive joints using the theory of cracks, *Int. Journal of Fracture* **1**, 114–118.

Mandelbrot, B.: 1983, *The Fractal Geometry of Nature*, W.H. Freeman, San Francisco.

Mandelbrot, B., Passoja, D. and Paullay, A.: 1984, Fractal character of fracture surfaces of metals, *Nature* **308**, 721–722.

Mecholsky, J. and Freiman, S.: 1991, Relationship between fractal geometry and fractography, *Journal of the American Ceramic Society* **74**(12), 3136–3138.

Mecholsky, J. and Mackin, T.: 1988, Fractal analysis of fracture in ocala chert, *Journal of Materials Science Letters* **7**, 1145–1147.

Mecholsky, J., Passoja, D. and Feinberg-Ringle, K.: 1989, Quantitative analysis of brittle fracture surfaces using fractal geometry, *Jour. Amer. Ceram. Soc.* **72**(1), 60–65.

Miller, M. and Gallagher, J.: 1981, An analysis of several fatigue crack growth rate (fcgr) descriptions, *in* S. Hudak Jr. and R. Bucci (eds), *Fatigue Crack Growth Measurements and Data Analysis, ASTM STP 738*, ASTM, Philadelphia, pp. 205–251.

Mindess, S. and Young, F.: 1981, *Concrete*, Prentice-Hall, Inc.

Måløy, K., Hansen, A., Hinrichsen, E. and Roux, S.: 1992, Experimental measurements of the roughness of brittle cracks, *Physical Review Letters* **68**(2), 213–215.

Mosolov, A.: 1991, Fractal j integral in fracture, *Soviet Technical Physics Letters* **17**(10), 698–700.

Mostovoy, e. a.: 1967, Use of crack-line loaded specimens for measuring plane strain fracture toughness, *J. of Materials* **2**(3), 661–681.

Murakami, Y.: 1987, *Stress Intensity Factors Handbook*, Pergamon Press. (2 Vols).

Newman, J.: 1971, An improved method of collocation for the stress analysis of cracked plates with various shaped boundaries, *Technical Report NASA TN D-6376*, National Aeronautics and Space Administration, Langley Research Center, Hampton, VA.

Newman, J. and Raju, I.: 1981, An emperical stress intensity factor equation for surface cracks, *Engineering Fracture Mechanics* **15**, 185–192.

Newton, R.: 1973, Degeneration of brick-type isoparametric elements, *Int. J. num. Meth. Engng.* **7**, 579–581.

Nikishkov, G. P. and Atluri, S. N.: 1987, Calculation of fracture mechanics parameters for an arbitrary three-dimensional crack, by the 'equivalent domain integral' method, *International Journal of Numerical Methods in Engineering* **24**(9), 1801–1821.

Saouma, V., Broz, J., Brühwiler, E. and Boggs, H.: 1991, Effect of aggregate and specimen size on fracture properties of dam concrete, *ASCE, Journal of Materials in Civil Engineering* **3**(3), 204–218.

Saouma, V., Dungar, R. and Morris, D. (eds): 1991, *Proceedings Dam Fracture*, Electric Power Research Institute (EPRI), Palo Alto, CA, Boulder.

Saouma, V., Natekar, D. and Sbaizero, O.: 2002, Nonlinear finite element analysis and size effect study of a metal-reinforced ceramics-composite, *Materials Science and Engineering A* **323**, 129–137.

Saouma, V. and Schwemmer, D.: 1984, Numerical evaluation of the quarter point singular element, *International Journal of Numerical Methods in Engineering* **20**, 1629–1641.

Saouma, V. and Sikiotis, E.: 1986, Stress intensity factors in anisotropic bodies using singular isoparametric elements, *Engineering Fracture Mechanics* **25**(1), 115–121.

Saouma, V. and Zatz, I.: 1984, An automated finite element procedure for fatigue crack propagation analyses, *Engineering Fracture Mechanics Journal* **20**(2), 321–333.

Saouma, V.E., Barton, C., and Gamal-El-Din, N.: 1990, Fractal Characterization of Cracked Concrete Surfaces, *Engineering Fracture Mechanics Journal* **35**(1), 47–53.

Saouma V.E., and Červenka, J. and Slowik, V. and Chandra Kishen, J.M.: 1994, Mixed mode fracture of rock-concrete interfaces, *in* Z. Bažant (ed.), *US-Europe Workshop on Fracture and Damage of Quasi-Brittle Materials: Experiment, Modeling and Computer Analysis*, Prague, Czech Republic.

Sha, G.: 1984, On the virtual crack extension technique for stress intensity factors and energy release rate calculation for mixed fracture modes, *Int. J. Fracture* **25**.

Shah, S. (ed.): 1984, *Application of Fracture Mechanics to Cementitious Composites*, Northwestern University. NATO Workshop.

Shah, S. P. and Jenq, Y. S.: 1985, A two parameter fracture model for concrete, *Journal of Engineering Mechanics Division, ASCE* .

Shah, S. and Swartz, S. (eds): 1989, *RILEM-SEM Int. Conference on Fracture Mechanics of Rock and Concrete*, Springer-Verlag, New-York.

Shih, C., de Lorenzi, H. and German, M.: 1976, Crack extension modelling with singular quadratic isoparametric elements, *Int. J. Fract.* **12**, 647–651.

Shih, C., Moran, B. and Nakamura, T.: 1986, Energy release rate along a 3-d crack front in a thermally stressed body, *Int. J. Fracture* **30**, 79–102.

Shing, P., Manzouri, T., Atkinson, R., Schuller, M. and Amadei, B.: 1994, Evaluation of grout injection techniques for unreinforced masonry structures, *Proc. of the Fifth U.S. National Conference on Earthquake Engineering, Vol. III*, Chicago, pp. 851–860.

Shirai, N.: 1993, Jci round robin analysis in size effect in concrete structures, *US-Japan Workshop on Fracture and Size Effect in Concrete*, Japan.

Sih, G.: 1974, Strain energy factors applied to mixed mode crack problems, *Int. J. Fracture* **10**.

Van Raan, A.: 1990, Fractal dimension of co-citation, *Nature* **347**, 626.

Červenka, J., Reich, R. and Saouma, V.: 1997–2003, Merlin, a three-dimensional finite element program based on a mixed-iterative solution strategy for problems in elasticity, plasticity, and linear and nonlinear fracture mechanics; user's manual, *Technical report*, Electric Power Research Institute (EPRI), Palo Alto; Tokyo Electric Power Service Company (TEPSCO), Tokyo. `http://civil.colorado.edu/~saouma/Merlin`.

Walker, E.: 1970, The effect of stress ratio during crack propagation and fatigue for 2024-t3 and 7075-t6 aluminum, *in* M. Rosenfeld (ed.), *Effects of Environment and Complex Load History on Fatigue Life*, ASTM STP 462.

Walsh, P.: 1972, Fracture of plain concrete, *Indian Concrete J.* **46**(11), 469–470 and 476.

Wells, A.: 1963, *Application of Fracture Mechanics at and Beyond General Yielding*, British Welding Research Ass., Report M13.

Westergaard, H.: 1939a, Bearing pressures and cracks, *J. Appl. Mech.* **61**.

Westergaard, H.: 1939b, Bearing pressures and cracks, *J. Appl. Mech.* **61**.

Wheeler, O.: 1972, Spectrum loading and crack growth, *J. of Basic Engineering* **94**, 181–186.

Wiberg, N.-E.: 1974, Matrix structural analysis with mixed variables, *International Journal of Numerical Methods in Engineering* **8**(2), 167–194.

Willenborg, J., Engle, R. and Wood, R.: 1971, A crack growth retardation model using an effective stress concept, *Technical report*, Air Force Flight Dynamics Laboratory Report, AFFDL-TM-71-1-FBR.

Williams, M.: 1952, Stress singularities from various boundary conditions in angular corners of plates in extension, *Jour. of Applied Mechanics, ASME* **19**(4), 526–528.

Williams, M.: 1957, On the stress distribution at the base of a stationary crack, *Jour. of Applied Mechanics, ASME* **24**(1), 109–114.

Williams, M. L.: 1959, The stresses around a fault or crack in dissimilar media, *Bulletin of the Seismological Society of America* **49**(2), 199–204.

Winslow, D.: 1985, The fractal nature of the surface of cement paste, *Cement and Concrete Research* **15**, 817–824.

Wittmann, F. (ed.): 1993, *Numerical Models in Fracture Mechanics of Concrete*, Balkema. Proceedings of the first Bolomey Workshop, Zurich, 1992.

Wittmann, F. H., (ed.): 1983, *Fracture Mechanics of Concrete*, Elsevier Science Publishers Company Inc. Proceedings of a Conference in Lausanne.

Wittmann, F., Rokugo, K., Brühwiler, E., Mihashi, H. and Simonin, P.: 1988, Fracture Energy and Strain Softening of Concrete as Determined by Means of Compact Tension Specimens, *Materials and Structures* **21**, 21–32.

Xu, S. and Reinhardt, H.: 1998, Crack extension resistance and fracture properties of quasi-brittle softening materials like concrete based on the complete process of fracture, *International Journal of Fracture* **92**, 71–99.